



저작자표시-비영리-변경금지 2.0 대한민국

이용자는 아래의 조건을 따르는 경우에 한하여 자유롭게

- 이 저작물을 복제, 배포, 전송, 전시, 공연 및 방송할 수 있습니다.

다음과 같은 조건을 따라야 합니다:



저작자표시. 귀하는 원저작자를 표시하여야 합니다.



비영리. 귀하는 이 저작물을 영리 목적으로 이용할 수 없습니다.



변경금지. 귀하는 이 저작물을 개작, 변형 또는 가공할 수 없습니다.

- 귀하는, 이 저작물의 재이용이나 배포의 경우, 이 저작물에 적용된 이용허락조건을 명확하게 나타내어야 합니다.
- 저작권자로부터 별도의 허가를 받으면 이러한 조건들은 적용되지 않습니다.

저작권법에 따른 이용자의 권리는 위의 내용에 의하여 영향을 받지 않습니다.

이것은 [이용허락규약\(Legal Code\)](#)을 이해하기 쉽게 요약한 것입니다.

[Disclaimer](#)

Doctoral Thesis

Ex vivo relaxation rates and magnetic susceptibility
changes of corpus callosum in aging rats :
Indicators of myelin

Hwapyeong Cho

Department of Biomedical Engineering

Ulsan National Institute of Science and Technology

2023

Ex vivo relaxation rates and magnetic susceptibility
changes of corpus callosum in aging rats :
Indicators of myelin

Hwapyeong Cho

Department of Biomedical Engineering

Ulsan National Institute of Science and Technology

Ex vivo relaxation rates and magnetic susceptibility
changes of corpus callosum in aging rats :
Indicators of myelin

A thesis/dissertation submitted to
Ulsan National Institute of Science and Technology
in partial fulfillment of the
requirements for the degree of
Doctor of Philosophy

Hwapyeong Cho

06.14.2023 of submission

Approved by

A handwritten signature in black ink, consisting of several loops and a long horizontal stroke, positioned above a solid horizontal line.

Advisor

Hyung Joon Cho

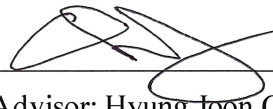
Ex vivo relaxation rates and magnetic susceptibility
changes of corpus callosum in aging rats :
Indicators of myelin

Hwapyeong Cho

This certifies that the thesis/dissertation of Hwapyeong Cho is approved.

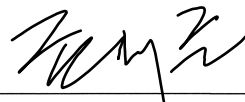
06.14.2023 of submission

Signature



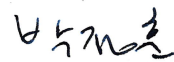
Advisor: Hyung Joon Cho

Signature



Taejoon Kwon

Signature



Jung-Hoon Park

Signature



Joon-Mo Yang

Signature



Kwangyeol Baek

Abstract

Myelin, the main component of white matter (WM), is a lipid-protein membrane structure that surrounds axon compactly in the nervous systems of vertebrates. Myelin exists in the form of a multi-lamellar sheath consisting of repeating units of the myelin bilayers and most of myelinated axons are distributed in WM. The main role of myelin is the electrical insulator for neurons, which increases the speed and efficiency of signal conduction. Since speed of action potential transmission is necessary to promote various neuronal functions, the measurements of myelin content are important for studies of normal development and neurodegenerative diseases.

In the evaluation of myelin, magnetic resonance imaging (MRI) is widely used as a noninvasive imaging technique that provides detailed anatomical images with various contrast mechanisms. Due to the limitation in MRI resolution and the size of myelinated axons ($\sim 1 \mu\text{m}$), myelin cannot be directly resolved by MRI. Also, the T_2 value of non-aqueous protons of myelin ($50 \mu\text{s} < T_2 < 1 \text{ms}$) is too short to measure the signal in conventional MRI, making direct imaging difficult. Therefore, most MRI techniques currently used for myelin imaging are mainly based on indirect estimation of myelin.

Currently, various MRI techniques for indirectly examining the myelin content are being studied with their respective strengths and weaknesses. However, there is still no method that is considered gold standard in the field of myelin MRI. Studies comparing and analyzing the effects of volumetric parameters on myelin through various validation methods are still lacking. Therefore, the purpose of this study is to quantify volumetric changes in myelin, such as myelin volume fraction (MVF), in the corpus callosum (CC) of post-mortem aging rat brains through MRI-based measurements and histological/theoretical validations.

In the first section, the relationship with MVF was established through the MRI-derived values: longitudinal relaxation rate R_1 and the magnetic susceptibility values obtained through quantitative susceptibility mapping (QSM). The absolute MVF values were determined by transmission electron microscopy (TEM) as a gold standard measure for comparison with the values obtained by the aforementioned MRI techniques. Also, QSM simulations were performed based on the TEM-derived structures to theoretically evaluate and understand the MR signal properties. Correlations of MVF versus MRI-derived values (R_1 and magnetic susceptibility) showed a strong linear relationship. In addition, QSM simulation results established a linearly proportional relationship between simulated magnetic susceptibility and MVF. Statistically significant linear correlations between MRI-derived values and MVF demonstrated that variable myelin content in WM (i.e., CC) could be quantified across different stages of aging. These results further support that both MRI techniques (R_1 and QSM) provide an efficient means to study the brain aging process with accurate volumetric quantification of myelin content in the WM.

In the second section, multiple spin echo sequence-based MRI- R_2 values were measured to confirm that myelin volume information could be detected even when the short- T_2 component (myelin water signal) was not detected due to the fixation effect. TEM-based quantification of MVF and corresponding Monte-Carlo simulation to estimate relaxation rates ($R_{2,IE}$) due to diffusion in the presence of inhomogeneous magnetic field perturbation in intra- and extra-cellular (IE) spaces were respectively performed. A significant correlation between mean MRI- R_2 and MVF values was observed, and the estimated $R_{2,IE}$ values of Monte-Carlo simulations in IE water signals were also positively correlated with MVF values. However, the magnitude of $R_{2,IE}$ values were much smaller than that those observed for MRI- R_2 values, indicating that R_2 -related changes in MVF are likely dominated by the myelin water content. Such comparisons between independent parameters from MRI, TEM, and simulations support the suggestion that myelin water signals were indistinguishably mixed to exhibit mono-exponential R_2 , and still reflect the volumetric information of myelin.

In conclusion, it was confirmed that the proposed MRI-based measurements (R_1 , R_2 and QSM) can be usefully used for the quantification of myelin volume in the post-mortem rat CC regions based on histological/theoretical validations (TEM and simulation).

Contents

Abstract	1-2
Contents	3
List of figures	4
List of tables	5
Chapter 1. Introduction	
1.1 Purpose	6
1.2 Outline	6
1.3 Abbreviations	6-7
Chapter 2. Background	
2.1 R_1 and R_2 relaxation	8-9
2.2 Quantitative susceptibility mapping	10-11
Chapter 3. Volumetric characterization of myelin by R_1 and magnetic susceptibility	
3.1 Introduction	12-14
3.2 Methods	14-17
3.3 Results	17-21
3.4 Discussion and Conclusions	22-26
Chapter 4. Access to the relationship between myelin volume fraction and R_2 measurement	
4.1 Introduction	27-28
4.2 Methods	29-33
4.3 Results	33-40
4.4 Discussion and Conclusions	40-44
Chapter 5. Conclusions	
5.1 Summary	45
5.2 Limitations and Future works	45
References	46-54
Acknowledgements	55

List of figures

Chapter 2. Background

2.1 R_1 and R_2 relaxation

Figure 2.1.1 Depiction of spins of protons	8
Figure 2.1.2 Change in net magnetization with a 90° radio frequency (RF) pulse	8
Figure 2.1.3 The recovery process of longitudinal magnetization	9
Figure 2.1.4 The loss process of transverse magnetization	9

2.2 Quantitative susceptibility mapping

Figure 2.2.1 Changes in magnetic field with change in magnetic susceptibility	10
Figure 2.2.2 Representation of MR signal and phase unwrapping theory	11

Chapter 3. Volumetric characterization of myelin by R_1 and magnetic susceptibility

Figure 3.1 Summary of the overall TEM sample preparation procedure	16
Figure 3.2 Summary of the overall TEM-based QSM simulation process	16
Figure 3.3 Representative MRI images	17
Figure 3.4 Qualities of ex vivo R_1 fitting	18
Figure 3.5 Summarized ex vivo R_1 and QSM measurements	18
Figure 3.6 TEM derived MVF and ex vivo MRI (R_1 and QSM) correlations	19
Figure 3.7 Simulation geometry to measure ΔB of the surrounding voxels	21
Figure 3.8 Simulation results and analyses	21
Figure 3.9 Hollow cylinder model simulation results and analyses	24

Chapter 4. Access to the relationship between myelin volume fraction and R_2 measurement

Figure 4.1 Brief description of how to calculate TEM-derived parameters from TEM image	31
Figure 4.2 The representative ex vivo MRI positioning and results	34
Figure 4.3 Mono-exponential fitting qualities	35
Figure 4.4 Multi-exponential relaxation fitting results	36
Figure 4.5 Histological verification process by TEM	36
Figure 4.6 The representative TEM images and correlation between each TEM-derived parameter	37
Figure 4.7 Schematic of the susceptibility anisotropy and diffusion of protons in simulation	38
Figure 4.8 Correlation analyses between parameters for each experiment: MRI, TEM, and simulation	39
Figure 4.9 Separation of the representative T_2 distributions by different T_2 -cutoff values	40
Figure 4.10 Multi-exponential relaxation fitting results using data in the TEM area	44

List of tables

Chapter 3. Volumetric characterization of myelin by R_1 and magnetic susceptibility

Table 3.1 Detailed TEM and MRI data analysis results of all samples	20
---	----

Chapter 4. Access to the relationship between myelin volume fraction and R_2 measurement

Table 4.1 MRI and TEM data analysis results of age groups	34
---	----

Table 4.2 Detailed MRI and TEM data analysis results of all samples	37
---	----

Chapter 1. Introduction

1.1 Purpose

The aim of this thesis is to quantify the volumetric change in myelin, such as myelin volume fraction (MVF), through magnetic resonance imaging (MRI)-based measurements and histological/theoretical validations. For the quantification of myelin by MRI, age-dependent changes in myelin in the corpus callosum (CC) of post-mortem rat brains were measured by several MRI techniques : R_1 , R_2 , and quantitative susceptibility mapping (QSM). Then, these changes are compared and analyzed based on histological verification through transmission electron microscopy (TEM) processing and theoretical verification through simulation processing.

In order to pursue the quantification of myelin based on these processes, the objectives of this thesis are as follows:

- (1) Volumetric characterization of myelin by R_1 and magnetic susceptibility
- (2) Access to the relationship between myelin volume fraction and R_2 measurement

1.2 Outline

The followings are a brief summary of each Chapter.

Chapter 2 introduces background on the MRI contrasts used in this thesis. The basic theories of relaxation rates (R_1 and R_2) and QSM techniques used to quantify myelin are discussed in this chapter.

Chapter 3 describes the relationship between MRI-based measurements (R_1 and QSM) and MVF, to evaluate age-related changes in myelin content using post-mortem rat brain samples. R_1 and magnetic susceptibility values are compared in the CC region of each sample, and these MRI results are verified by TEM-based MVF analysis and QSM simulation results.

Chapter 4 describes the characterization of myelin volume fraction through MRI- R_2 measurements to access age-related changes in myelin content using post-mortem rat brain samples. R_2 values derived from the CC region of each sample are evaluated for how much myelin volume information is included through TEM-based MVF analysis and field perturbation simulation results.

Chapter 5 contains the summary and conclusions of this thesis.

1.3 Abbreviations

ADC	Apparent diffusion coefficient
CC	Corpus callosum
EM	Electron microscopy

FOV	Field of view
FPM	Finite perturber method
GA	Glutaraldehyde
IE	Intra- and extra-cellular
MERA	Multi-exponential relaxation analysis
MGE	Multi gradient echo
MRI	Magnetic resonance imaging
MST	Myelin sheath thickness
MT	Magnetization transfer
MTR	Magnetization transfer ratio
MVF	Myelin volume fraction
MWF	Myelin water fraction
MWI	Myelin water imaging
NA	Number of averages
NNLS	Nonnegative least-squares
PBS	Phosphate buffered saline
PFA	Paraformaldehyde
PND	Postnatal day
PNM	Postnatal month
QSM	Quantitative susceptibility mapping
RARE-VTR	Rapid acquisition with relaxation enhancement with variable repetition time
RF	Radio frequency
ROI	Region of interest
SEM	Scanning electron microscopy
TE	Echo time
TEM	Transmission electron microscopy
TR	Repetition time
UTE	Ultrashort echo time
WM	White matter

Chapter 2. Background

2.1 R_1 and R_2 relaxation

MRI is a non-invasive imaging technique that can acquire various anatomical and functional images using an applied magnetic field and radio frequency (RF) signals [1]. MRI acquires images by changing the arrangement of protons (Hydrogen; ^1H) in the body. If there is no external magnetic field (B_0), protons are randomly oriented and magnetization is canceled, so net magnetization (M_0) does not occur. At this time, when a large B_0 is applied to the protons, the protons are aligned in the same direction as B_0 to form a non-zero M_0 as shown in Figure 2.1.1.

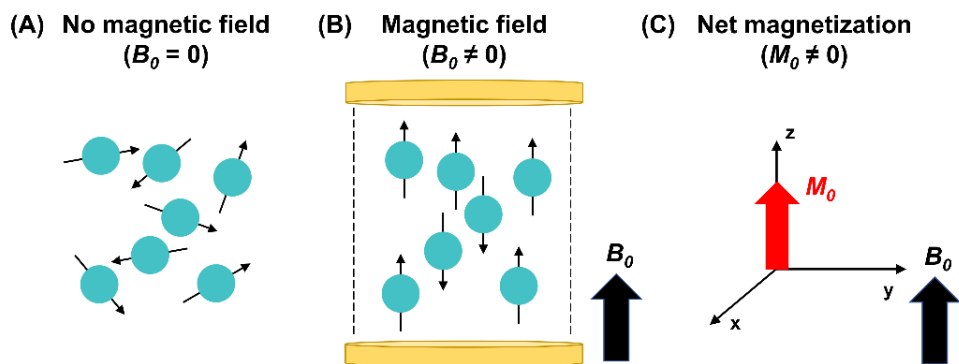


Figure 2.1.1. Depiction of spins of protons. (A) Randomly oriented spins in the absence of an external magnetic field (B_0). (B) Spins oriented parallel to B_0 in the presence of B_0 . (C) Formation of net magnetization (M_0 ; red arrow) by B_0 .

To obtain the magnetic resonance (MR) signal, an RF pulse must be applied to generate a resonance that changes the direction of M_0 . When an 90° RF pulse is applied, longitudinal magnetization (M_z) disappears and only transverse magnetization (M_{xy}) remains as shown in Figure 2.1.2.

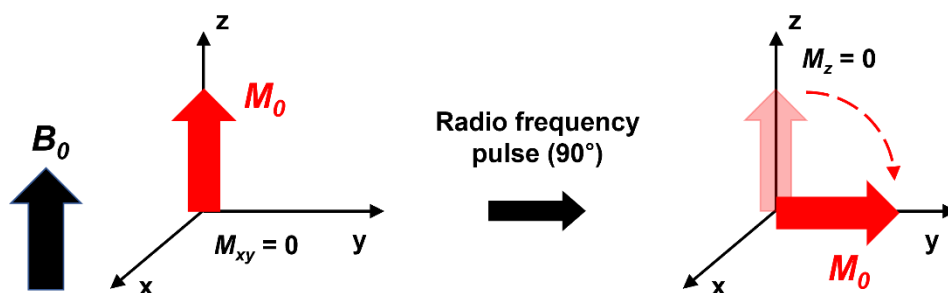


Figure 2.1.2. Change in net magnetization (M_0 ; red arrow) with a 90° radio frequency (RF) pulse.

After resonance state, M_0 returns to its original equilibrium state, called relaxation, and relaxation is divided into two independent types. The recovery of M_z is an exponential process with a time constant T_1 , the time required for magnetization to reach 63% of its maximum value as shown in Figure 2.1.3. R_1 , called longitudinal relaxation rate and defined as reciprocal of T_1 , is the rate at which excited protons give up their energy and return to the equilibrium state. Also, the decay of transverse magnetization is an exponential process with a time constant T_2 , the time required for magnetization to fall to 37% of its initial value as shown in Figure 2.1.4. R_2 , called transverse relaxation rate and defined as reciprocal of T_2 , is the rate at which MR signal decays away due to spins interacting with one another. R_1 and R_2 are known as the basic contrast mechanisms of MRI, and in this thesis, these values were analyzed to quantify myelin in post-mortem brain tissue.

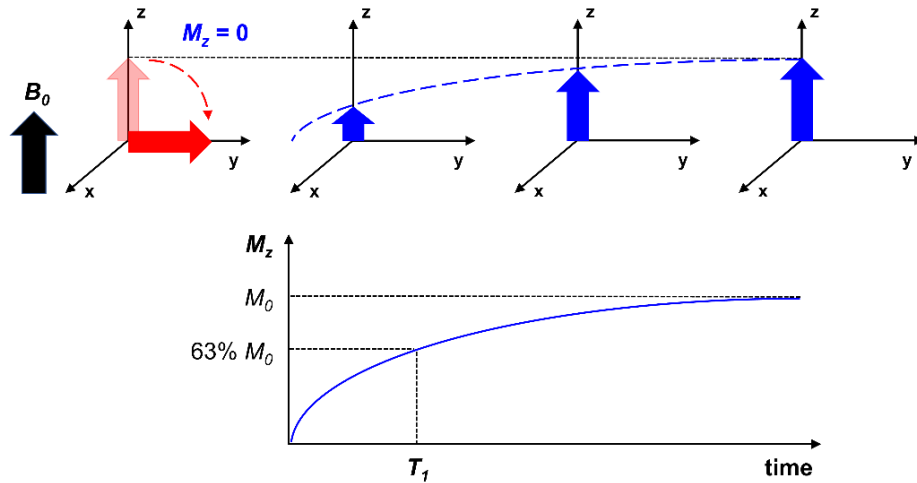


Figure 2.1.3. The recovery process of longitudinal magnetization (M_z ; blue arrow).

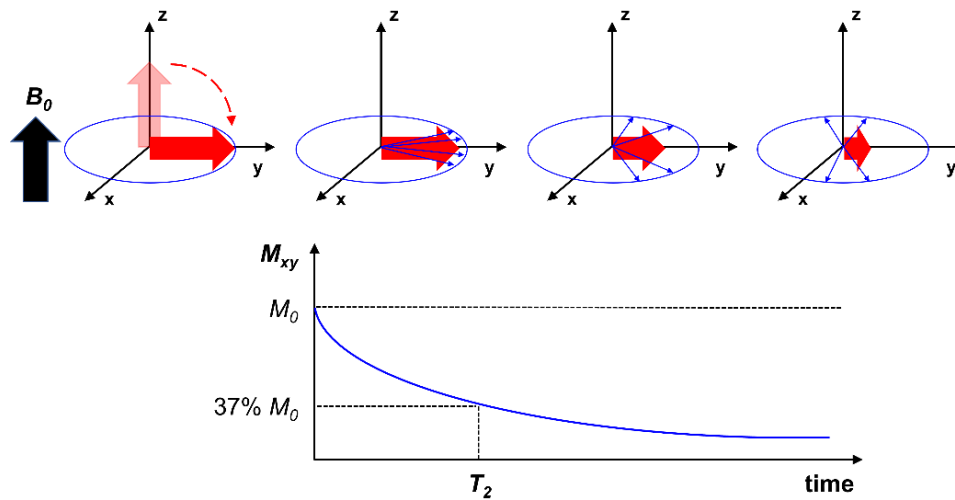


Figure 2.1.4. The loss process of transverse magnetization (M_{xy} ; red arrow).

2.2 Quantitative susceptibility mapping

Magnetic susceptibility is a dimensionless intrinsic property of a material that measures how much a material becomes magnetized in an external magnetic field. Depending on whether this value is negative or positive, it can be divided into two categories: diamagnetic and paramagnetic. A material is diamagnetic if its magnetic susceptibility is negative, in which case magnetic field is weakened by induced magnetization. Also, a material is paramagnetic if its magnetic susceptibility is positive, in which case magnetic field is strengthened by induced magnetization. These effects of magnetic susceptibility are shown in Figure 2.2.1. Examples of major diamagnetic sources include myelin and calcium, and examples of major paramagnetic sources include iron and gadolinium. Myelin and iron are each major markers in neurodegenerative diseases, and how to differentiate between paramagnetic and diamagnetic materials in images is an important problem in medical imaging.

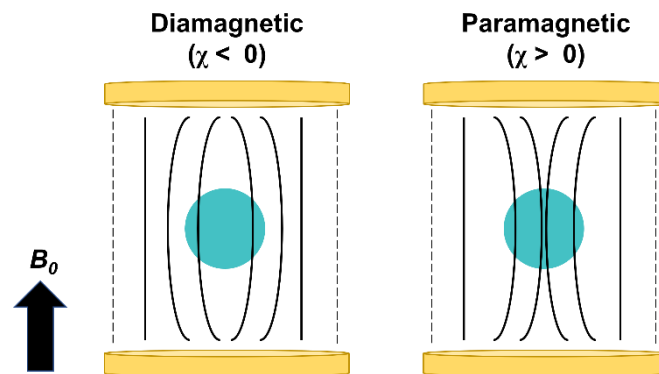


Figure 2.2.1. Changes in magnetic field with change in magnetic susceptibility (χ).

Phase information provides clues for imaging a material's magnetic susceptibility. In MRI, signal can be represented as a complex number, with real and imaginary components. Each data point can be defined as magnitude and phase shown in Figure 2.2.2A. In many MRI applications cases, the reconstruction cares about magnitude and ignores phase part. However, since paramagnetic and diamagnetic materials produce different phase shifts in MRI data, the effect of magnetic susceptibility can be distinguished using phase information. In MRI, phase values outside the $-\pi$ to π range are wrapped so that values greater than π return to the negative axis and vice versa. Therefore, the actual phase value may be different from the detected phase, and a technique called phase unwrapping is applied to obtain the actual phase value as shown in Figure 2.2.2B. These unwrapped phase data are used for magnetic susceptibility measurements.

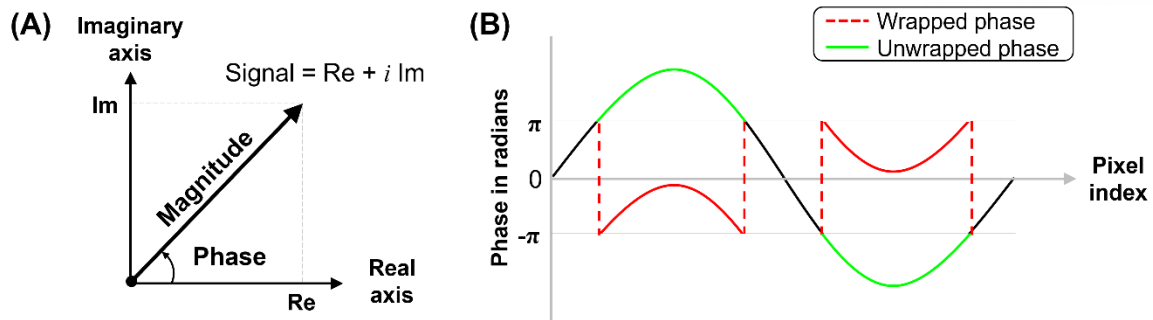


Figure 2.2.2. Representation of MR signal and phase unwrapping theory. (A) Complex MR signal with real and imaginary parts. (B) Example of wrapped (red) and unwrapped (green) phase data.

Quantitative susceptibility mapping (QSM) is a novel MRI technique that measures the spatial magnetic susceptibility distribution of a sample from unwrapped phase data [2]. In MRI, magnetic susceptibility distribution of the sample causes a magnetic field perturbation by an applied magnetic field, and phase information is measured from this perturbation. However, QSM technique reconstructs the magnetic susceptibility distribution from the phase information by solving the inverse problem [2,3]. In QSM, the bulk magnetic susceptibility of each voxel is calculated as the weighted sum of the magnetic susceptibility values of the components and their relative volume fractions. Capturing the diamagnetic properties of myelin via QSM indicates that it could be another method for the quantification of myelin. Therefore, in this thesis, QSM is used to access myelin content in post-mortem brain tissue through MRI.

Chapter 3. Volumetric characterization of myelin by R_1 and magnetic susceptibility

3.1 Introduction

The myelin is a lipid-rich substance that surrounds the axons of nerve cells in both the central and peripheral nervous systems of vertebrates [4,5]. The myelin sheath exists in the form of multilamellar layers consisting of repeating units of myelin lipid bilayers. Most myelinated axons are distributed in the white matter (WM) [6–8], in which myelin mainly functions as an electrical insulator of neurons that increases the signal conduction speed [4,6]. Because the speed of actual potential transmission is necessary to promote various neuronal functions, the development of the myelin sheath content in the aging brain is of great interest [9,10].

In the evaluation of myelin, magnetic resonance imaging (MRI) is widely used as a noninvasive imaging technique that provides multiple contrast mechanisms. Several quantitative techniques, such as magnetization transfer (MT) imaging and myelin water imaging (MWI), have been developed [10–13]. However, these MRI methods have several shortcomings. For instance, MT effects are dependent upon the relative contrast derived from the off-resonance radio frequency (RF) power and frequency offset parameters, which makes it less attractive for absolute quantification [12]. By contrast, MWI requires multiexponential fitting procedures, which may be susceptible to noise and fitting routines [12]. In particular, in *ex vivo* analysis, MT effects and multiexponential transverse relaxation behaviors (for MWI) may be altered by the fixation process of brain samples. Post-mortem formalin-fixed brains showed significant changes in the MT ratio (MTR), which weakened the association between MT effects and myelin content [14]. A post-mortem MWI study also showed that the T_2 distribution can be altered, probably because of myelin sheath loosening, cell shrinkage, and changes in various water compartments during the fixation process [15,16].

On the other hand, absolute quantitative susceptibility mapping (QSM) and T_1 mapping may provide reliable and accurate metrics, especially for the myelin volume fraction (MVF) of *ex vivo* brains, as both values were modeled to be linearly proportional to myelin content [17]. Previously, in a post-mortem human study, Stueber et al. introduced a linear function model of T_1 with a dominant myelin concentration and showed that T_1 was strongly influenced by MVF [17]. T_1 mapping also confirmed high colocalization with myelinated regions and was used to assess the brain cortical myelination [12,18]. In the case of the QSM study, the magnetic susceptibility (χ) obtained from QSM shows linear relationships with diamagnetic myelin and paramagnetic iron contents, suggesting that magnetic susceptibility may be an important indicator of MVF in the WM, where most myelinated fibers are

distributed [17]. An in vivo QSM study on humans found changes in susceptibility to WM caused by myelination during brain development [19]. For rodents, an ex vivo comparison study between QSM and histology data (Luxol Fast Blue myelin staining) of mice (C57BL/6 mice, postnatal days [PND] 2–56) showed that the magnetic susceptibility of the WM becomes more diamagnetic as the brain develops, and these changes in magnetic susceptibility are correlated with the intensity of myelin staining in the early developmental stage [20]. Another in vivo comparison between the MRI phase and histology (black gold II myelin staining) during early development in rats (Wistar rats, PND 3–40) showed that changes in phase contrast during development were well correlated with the optical intensity of histology data [21].

As observed in previous studies, both QSM and R_1 methods are strong candidates for the measurement of myelin content and can facilitate the quantification process with proper validation. To confirm the reliability of these MRI-based myelin content quantification methods, careful verification is required through reference standard methods such as histology or electron microscopy (EM). EM is known to be one of the most reliable methods for measuring myelin content, because it has sufficient resolution to directly image the myelin structure. It is important to note that two studies have identified changes in myelin structures caused by aging in rodents using EM images [22,23]. Both scanning EM (SEM) studies of the optic nerves of mice (C57BL/6 J mice, postnatal month [PNM] 1 and 12) and transmission EM (TEM) studies in the pyramidal tract and spinal posterior funiculus of rats (Sprague Dawley rats, PND 14–PNM 26) have identified age-related volumetric and structural changes in myelin [22,23]. However, these studies presented cross-sectional time point measurements of myelin content, while other previous MRI myelin studies in rodents were only performed in the early developmental stage. To date, few studies have evaluated changes encompassing adolescence to middle and old age in rodents, with confirmation through the correlation between MRI and histological methods. In particular, in gerontology, the mapping of age-related changes in myelin content, especially defining the relationship between MRI- and EM-derived MVF parameters, should be of substantial help in understanding the myelin degradation process in the aging brain.

In this study, our central objectives were (i) to establish and validate the relationship between MRI-based measurements (QSM and R_1) and EM-derived MVF, and (ii) to assess age-related changes in myelin content via ex vivo rat brain samples collected up to 20 months after birth. For this purpose, ex vivo MRI and TEM experiments were conducted to determine the relationship between MRI-derived R_1 ($1/T_1$) and QSM data and the corresponding absolute MVF values, respectively, for 6 weeks ($n = 3$), 4 months ($n = 3$), and 20 months ($n = 3$) in the corpus callosum (CC) of normally aging ex vivo rat brains. Finite perturber method (FPM)-based simulations geometrically reconstructed using TEM data were performed to relate the magnetic field shift (ΔB) changes with respect to myelin structure, such as

MVF. Both theoretically and experimentally, the current investigation presents strong support for MRI-derived volumetric quantification methods in assessing absolute myelin content in aging WM.

3.2 Methods

3.2.1 Animal preparations

Three young (6-week-old), three adult (4-month-old), and three old (20-month-old) female Sprague Dawley rats were used for the experiments with the approval of the Institutional Animal Care and Use Committees (IACUC) of Ulsan National University of Science and Technology. Young rats were obtained from Orient Bio (Gyeonggi, Republic of Korea), while adult and old rats were obtained from the Aging Tissue Bank (Pusan National University, Republic of Korea). All rats were anesthetized with isoflurane and intracardially perfused with saline solution and 10% neutral buffered formalin. After heart perfusion, to prevent brain tissue damage that may occur when extracting the brain from the skull, the brain was extracted with the skull and immediately fixed in 10% neutral buffered formalin. The samples were then placed in a formalin-filled 30-mL syringe and adjusted so that the fiber direction in the CC was perpendicular to the main magnetic field.

3.2.2 MRI experiments and postprocessing

Three young All studies were performed using a 7 T MRI scanner (Bruker, Germany) with a 40 mm volume coil. The R_f maps were acquired using a rapid acquisition with relaxation enhancement with variable repetition time (RARE-VTR) sequence with the following parameters [24] : repetition time (TR) = 50, 100, 200, 300, 500, 700, 1000, 2000, 3000, and 5000 ms; TE = 8 ms; RARE factor = 1; matrix size = 256×256 pixels; field of view (FOV) = 25×25 mm²; number of averages (NA) = 4; number of slices = 1; and slice thickness = 0.4 mm (total scan time : 3 hours 39 minutes). For the QSM reconstruction, gradient echo data were acquired using a multi gradient echo (MGE) sequence with the following parameters : TR = 4000 ms; TE = 2.7–50.3 ms (echo images = 15, echo spacing = 3.4 ms); flip angle = 90°; matrix size = 256×256 ; FOV = 25×25 mm²; NA = 4; number of slices = 20; and slice thickness = 0.4 mm (total scan time : 1 hours 8 minutes). The slices that were consistently matched with the R_f measurement were used for the following QSM analysis.

Voxel-wise R_f values were estimated by nonlinear least-squares data fitting using the function $S(t) = S_0 \times (1 - e^{-t/T1})$, where $S(t)$ is the time-dependent signal intensity at time t and S_0 is the fully recovered signal intensity.

QSM algorithms were implemented using the following steps: selection of the three shortest TEs (2.7, 6.1, and 9.5 ms); temporal phase unwrapping followed by a weighted linear least-square fitting [25]; Laplacian-based spatial phase unwrapping [26]; total field acquisition; removal of the background field

using the Laplacian boundary value method [27]; and deconvolution of the magnetic field with the dipole kernel to solve the field-to-source inverse problem by the morphology-enabled dipole inversion method [28]. The reason for calculating QSM by selecting the shortest TEs in this process is to obtain high signal-to-noise susceptibility maps. For QSM quantification, the mean of the whole brain was used as a reference.

Among the WM regions, the CC was selected as the region of interest (ROI) because it is the largest WM structure in the brain [29]. Each ROI voxel was classified into its age group (young, adult, or old), and then averaged for mean and histogram analyses. The Kruskal–Wallis test with Bonferroni correction was used to identify statistical differences between the age groups. All postprocessing steps were performed using MATLAB (MathWorks).

3.2.3 TEM processing

After the MRI experiment, the CC from the brain was extracted and cut into 1 mm^3 tissue blocks from the same slice used for MRI. The cut samples were fixed in 1% osmium tetroxide in phosphate buffer, dehydrated in a graded series of ethanol to propylene oxide, embedded in Eponate 12 resin (Ted Pella Inc., Redding, USA), and cured in an oven at $60 \text{ }^\circ\text{C}$. The samples were then sliced into ultra-thin sections (approximately 100 nm) using an ultramicrotome (EM UC7, Leica) and imaged on a TEM (Tecnai G2 F20 X-Twin, FEI) operated at 200 kV. The sample preparation procedure is shown in Figure 3.1. For MVF analysis, 3–7 images were collected per animal with a magnification factor of 2,300. Approximately 60–150 myelinated axons were measured in each image. Each myelinated axon was segmented using GIMP (<https://www.gimp.org/>), and MVF calculations were performed using MATLAB. The myelin segmentation method was performed according to the procedure of [30].

3.2.4 Simulation

FPM-based simulations were performed to investigate the effects of the structural factors of a voxel affected by neighboring voxels [31]. This was motivated by the notion that voxel-wise magnetic susceptibility estimation in QSM depends on the phase accumulation in neighboring voxels, as well as the central voxel [32]. Each TEM image (matrix size = 2048×2048 pixels) was under-sampled to 200×200 pixels, stacked to form a 3D TEM image matrix (matrix size = $200 \times 200 \times 200$ voxels, unit voxel length = $0.04 \text{ }\mu\text{m}$), and located at the center of an empty space (matrix size = $600 \times 600 \times 600$ voxels). Myelinated axon structures were distributed in the matrix in a perpendicular orientation with respect to the main magnetic field ($\theta = 90^\circ$; θ is the angle between the myelinated axon and the magnetic field). The ΔB map was calculated by FPM with magnetic field strength (B_0) = 7 T; magnetic susceptibility of myelin = -0.13 ppm [31,33]. The resulting ΔB map was under-sampled to $3 \times 3 \times 3$ voxels with a unit

voxel length of $8\ \mu\text{m}$ to consider TEM image portion as single voxel. For zero-padding process, under-sampled ΔB map was located at the center of the empty space (matrix size = $101 \times 101 \times 101$ voxels). Subsequently, QSM algorithms were implemented using deconvolution of the ΔB map with the dipole kernel to solve the field-to-source inverse problem by dipole inversion with total variation regularization [34]. Only one center voxel of the resulting QSM map was used for analysis to match that of the corresponding MRI QSM image. This TEM-based QSM simulation process is described in Figure 3.2.

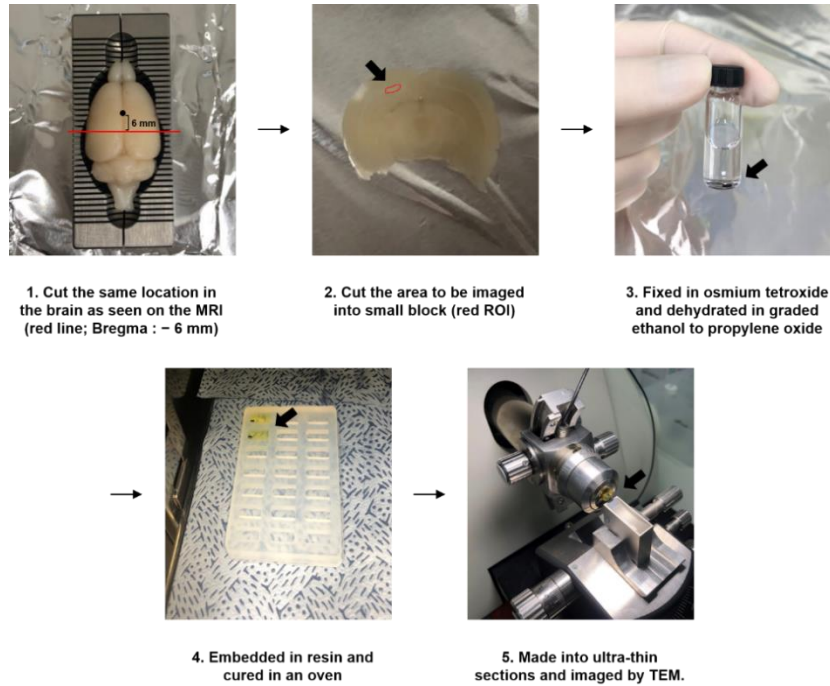


Figure 3.1. Summary of the overall TEM sample preparation procedure.

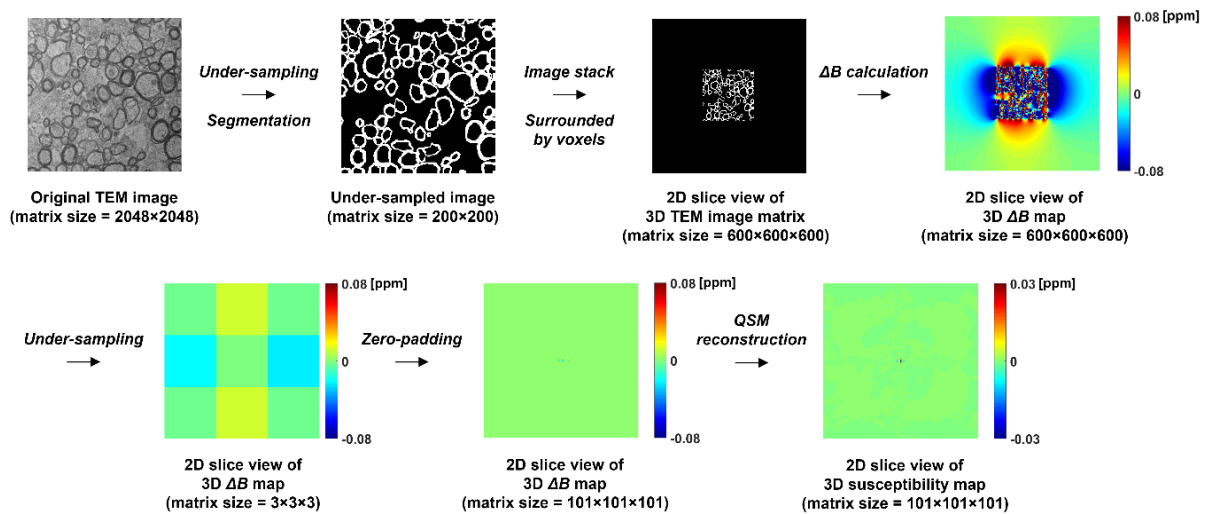


Figure 3.2. Summary of the overall TEM-based QSM simulation process.

Additionally, simulations were performed on a hollow cylinder model to investigate the anisotropic susceptibility effect of myelin on the relationship between QSM and MVF [35]. A hollow cylinder structure was created with a matrix size of $101 \times 101 \times 101$ voxels (unit voxel length = $0.02 \mu\text{m}$), where the outer radius length was maintained at 50 voxels. Five cases with different g-ratio and MVF values were used to measure the structural effects from the equation: g-ratio = 0.9 (MVF = 15%); g-ratio = 0.8 (MVF = 28%); g-ratio = 0.7 (MVF = 39%); g-ratio = 0.6 (MVF = 49%); and g-ratio = 0.5 (MVF = 58%). After setting the structures, the resulting matrix was centered in an empty space (matrix size = $303 \times 303 \times 303$ voxels). Two different contrast mechanisms, hollow cylinder models formed from a material that considers only isotropic susceptibility, while both isotropic + anisotropic susceptibilities were used with the following parameters: isotropic susceptibility (χ_I) = -0.12 ppm; anisotropic susceptibility (χ_A) = -0.12 ppm; $B_0 = 7$ T; and $\theta = 90^\circ$ [35]. The ΔB map calculations were conducted analytically following a previous report [35]. Subsequently, QSM simulation followed identical processes, which were used for TEM myelin images as described in the above paragraph.

3.3 Results

Representative ex vivo R_1 mapping and QSM results of the 6 week-, 4-, and 20 month axial brains (Bregma: -6 mm) are shown in Figure 3.3. The area of the CC is indicated by the red line in Figure 3.3A. The increase in R_1 and the decrease in magnetic susceptibility values with aging were apparent in the CC (Figures. 3.3B and 3.3C). Most of the R -squared (R^2) values for ex vivo data fitting of R_1 values exceeded 0.96, as indicated by the representative R^2 maps (Figure 3.4A). The representative voxel fitting curves showed a significant increase in R_1 values from RARE-VTR signal curves with the aging CC (Figure 3.4B).

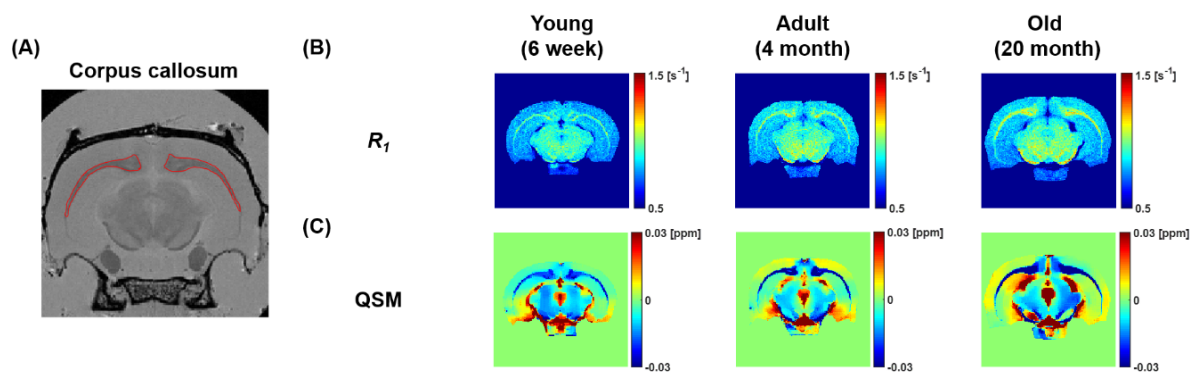


Figure 3.3. Representative MRI images. (A) Proton density-weighted image with ROI of the CC region (red). Representative (B) R_1 maps and (C) QSM results of rats in young (6 weeks), adult (4 months), and old (20 months) groups.

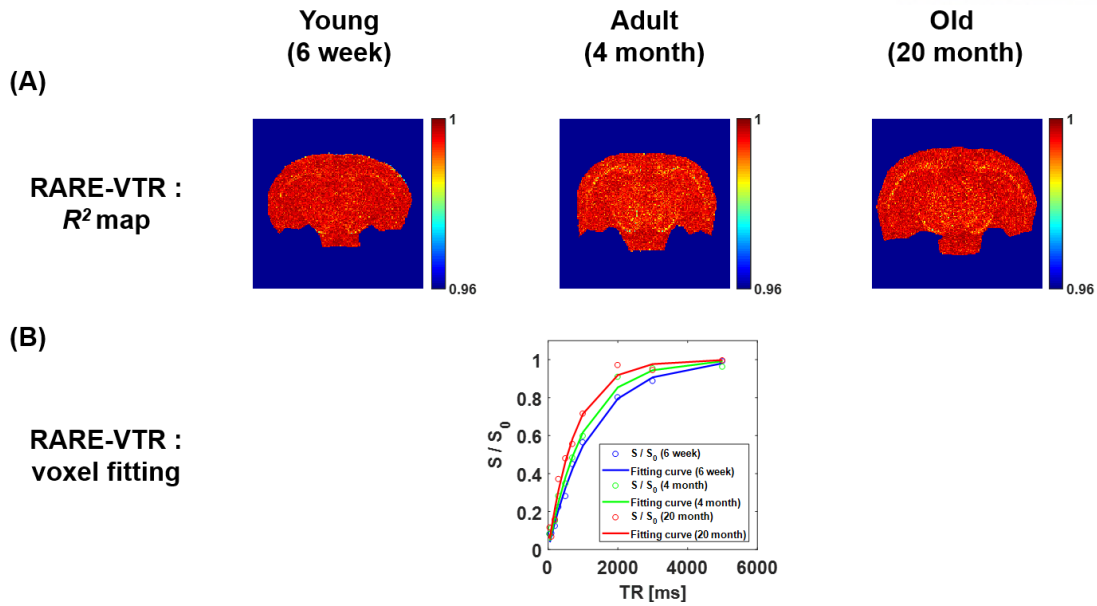


Figure 3.4. Qualities of ex vivo R_1 fitting. RARE-VTR sequence: (A) representative R^2 maps and (B) representative voxel fitting curves in CC regions of young (blue), adult (green), and old (red) groups.

All ex vivo R_1 and QSM measurements are shown in Figure 3.5. Mean R_1 values significantly increased with age ($p < 0.0001$, Kruskal–Wallis test followed by Bonferroni correction), as shown by the violin plots in Figure 3.5A. Mean magnetic susceptibility values significantly decreased with aging ($p < 0.0001$, Kruskal–Wallis test followed by Bonferroni correction), as shown by the violin plots in Figure 3.5B. The rates of such changes appear to slow down in the aging stage (adult to old section) for both R_1 and magnetic susceptibility values and can be clearly identified by comparing the slopes of the trend line for each interval. A negative linear relationship was found between R_1 and the magnetic susceptibility values in the CC regions. The correlation (Pearson's correlation coefficient $r = -0.8673$; $p < 0.01$) between mean R_1 and magnetic susceptibility values for each case is shown in Figure 3.5C.

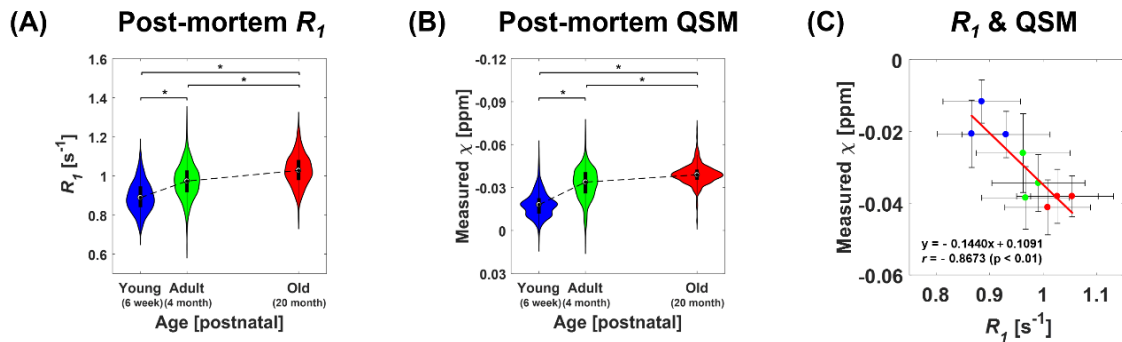


Figure 3.5. Summarized ex vivo R_1 and QSM measurements. Histogram distributions (violin plots) of measured (A) R_1 and (B) χ for young (6 weeks), adult (4 months), and old (20 months) age groups

(Kruskal-Wallis; $p < 0.0001$ is denoted as *). Dotted trend lines in the histograms connect corresponding median values of each group. Scatter plot between R_I and QSM data using (C) mean values ($y = -0.1440x + 0.1091$; $r = -0.8673$; $p < 0.01$) with linear fit lines. Blue dots: young groups, green dots: adult groups, red dots: old groups.

Representative raw TEM images and corresponding myelin sheath segmented images of 6 week-, 4-, and 20 month old CCs are shown in Figure 3.6A. In the segmented TEM images, myelin sheaths and axons were red- and white-colored. It can be clearly observed that the volume fractions of myelinated regions increase substantially with aging, as shown in Figure 3.6A. The scatterplot between mean MVF (MVF_{mean}) and MRI-derived mean R_I data ($R_{I,\text{mean}}$) for nine cases is shown in the top panel of Figure 3.6B ($R_{I,\text{mean}} = 0.7948 \times MVF_{\text{mean}} + 0.8118$, $r = 0.9138$; $p < 0.01$). The scatterplot between mean MVF and MRI-derived mean χ ($\chi_{\text{measured,mean}}$) values are also shown in the bottom panel of Figure 3.6B ($\chi_{\text{measured,mean}} = -0.1218 \times MVF_{\text{mean}} - 0.006345$, $r = -0.8435$; $p < 0.01$). MVF values tended to increase with age, ranging from 10% to 30%. $R_{I,\text{mean}}$ values ranged from 0.86 to 1.05 (1/s), and $\chi_{\text{measured,mean}}$ values ranged from -0.012 to -0.041 (ppm). Detailed MRI- and TEM-derived values are summarized in Table 3.1.

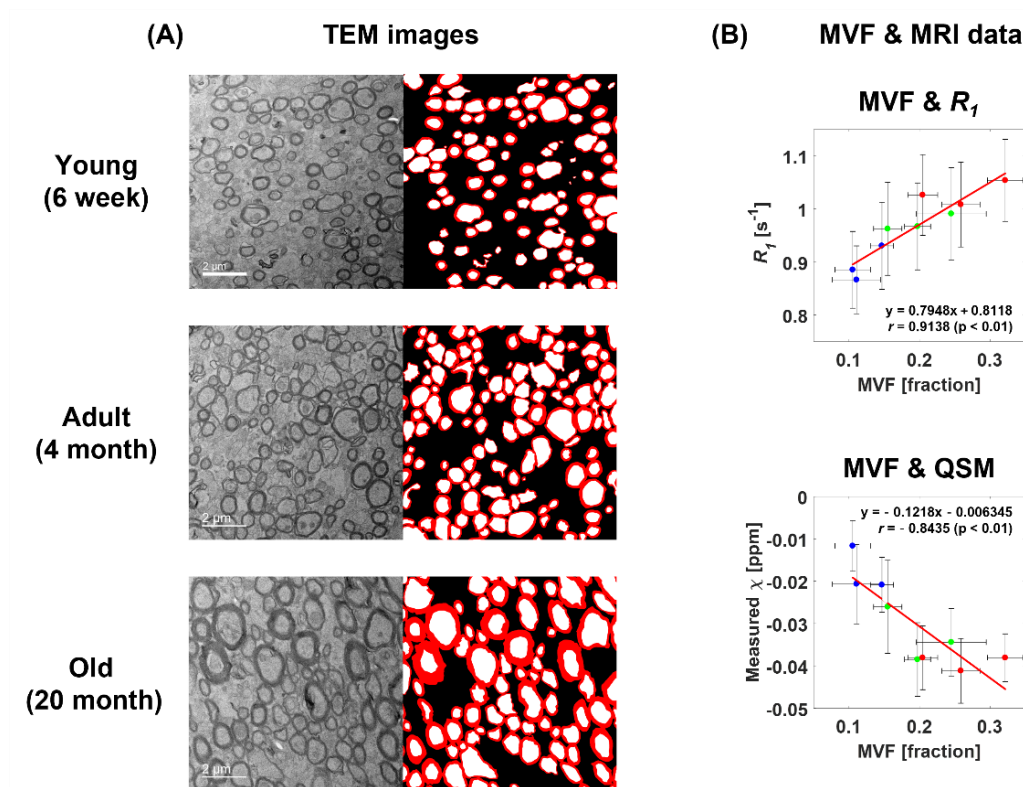


Figure 3.6. TEM derived MVF and ex vivo MRI (R_I and QSM) correlations. (A) Representative TEM images (left) and segmented TEM images (right) of young (6 weeks), adult (4 months), and old (20

months) age groups. Scale bar = 2 μm . In segmented images, each area is divided by color (background: black; axon: white; myelin sheath: red). (B) Scatter plots of mean MVF & mean R_f data (top; $y = 0.7948x + 0.8118$; $r = 0.9138$; $p < 0.001$), and mean MVF & mean QSM data (bottom; $y = -0.1218x - 0.006345$; $r = -0.8435$; $p < 0.01$) with linear fit lines. Blue dots: young groups, green dots: adult groups, red dots: old groups.

Age [postnatal]	6 week-1	6 week-2	6 week-3	4 month-1	4 month-2	4 month-3	20 month-1	20 month-2	20 month-3
Mean MVF [fraction]	0.1466 (± 0.0164)	0.1107 (± 0.0344)	0.1056 (± 0.0251)	0.2450 (± 0.0495)	0.1549 (± 0.0201)	0.1971 (± 0.0185)	0.2585 (± 0.0269)	0.3214 (± 0.0252)	0.2045 (± 0.0212)
Number of slices	7	3	4	7	3	4	4	7	3
R_f [s^{-1}]	0.9306 (± 0.0824)	0.8665 (± 0.0639)	0.8853 (± 0.0724)	0.9911 (± 0.0869)	0.9626 (± 0.0878)	0.9671 (± 0.0820)	1.0085 (± 0.0800)	1.0541 (± 0.0775)	1.0265 (± 0.0762)
Magnetic susceptibility [ppm]	-0.0209 (± 0.0065)	-0.0207 (± 0.0094)	-0.0117 (± 0.0060)	-0.0344 (± 0.0079)	-0.0261 (± 0.0110)	-0.0385 (± 0.0087)	-0.0412 (± 0.0077)	-0.0381 (± 0.0056)	-0.0381 (± 0.0075)

Table 3.1. Detailed TEM and MRI data analysis results of all samples.

The geometries of the FPM-based simulations are shown in Figure 3.7. Each TEM image was reconstructed into a 3D image and centered in $26\times$ larger adjacent spaces to compute the ΔB map (Figure 3.7). Representative TEM-based images and calculated the ΔB maps of 6 week-, 4-, and 20 month old CC are shown in Figure 3.8A. It can be seen that as MVF changes with age, it also affects the ΔB values (Figure 3.8A). The scatterplot between QSM simulation-derived χ ($\chi_{\text{simulated}}$) versus the corresponding MVF value of each TEM image is shown in the top panel of Figure 3.8B ($\text{MVF} = -5.7359 \times \chi_{\text{simulated}} + 0.01393$, $r = -0.9648$; $p < 0.01$). The scatterplot between QSM simulation-derived mean χ ($\chi_{\text{simulated,mean}}$) values from TEM images versus the corresponding $\chi_{\text{measured,mean}}$ values from MRI are also shown in the bottom panel of Figure 3.8B ($\chi_{\text{measured,mean}} = 0.7472 \times \chi_{\text{simulated,mean}} - 0.006144$, $r = 0.8958$; $p < 0.01$) for nine cases. Simulated χ values ranged from -0.008 to -0.057 ppm and tended to decrease negatively with aging. It can be seen that the range of the simulated χ values is similar to the measured χ values.

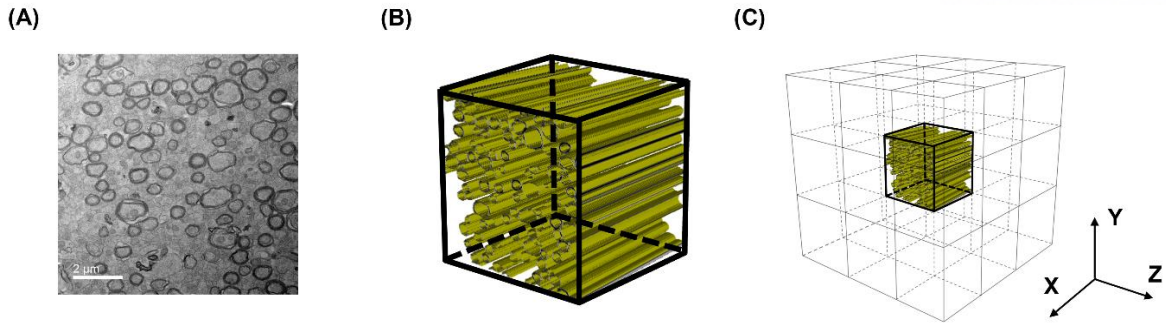


Figure 3.7. Simulation geometry to measure ΔB of the surrounding voxels. (A) The representative TEM image, (B) 3D reconstructed views of TEM image, and (C) entire TEM-based simulation geometry matrix in the young (6 week) age sample.

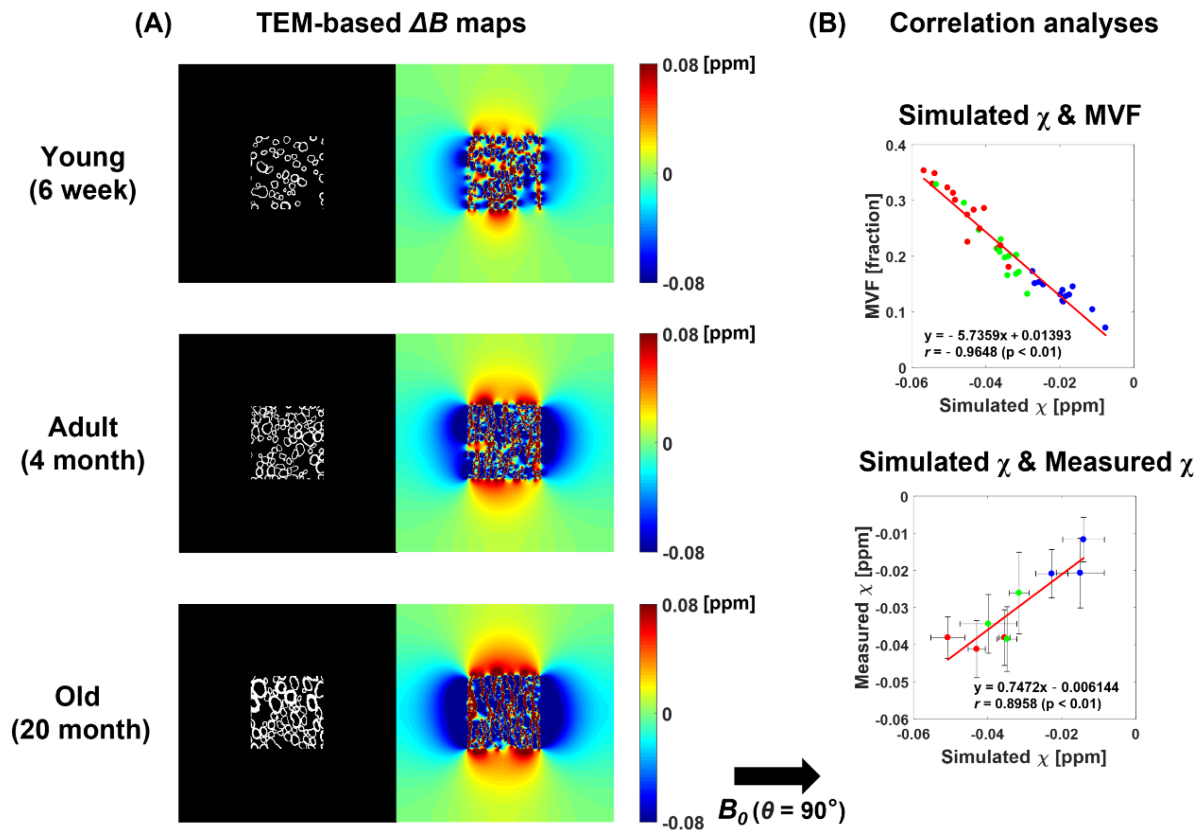


Figure 3.8. Simulation results and analyses. (A) 2D slice views of representative TEM-based simulated images (left) and simulated ΔB maps (right) of young (6 weeks), adult (4 months), and old (20 months) age groups. These TEM-based myelin cylinders aligned perpendicular to B_0 ($\theta = 90^\circ$). (B) Scatter plots of simulated χ & MVF data ($r = -0.9648$; $p < 0.01$) and mean simulated χ & mean measured χ data ($r = 0.8958$; $p < 0.01$) with linear fit lines. Blue dots: young groups, green dots: adult groups, red dots: old groups.

3.4 Discussion and Conclusions

To date, MRI-based myelin studies in rodent models have been conducted and are primarily available to investigate the early stages of WM development with associated histological validations [20,21]. On the other hand, studies of the aging effects on myelin beyond the developmental stages are rare, and only recently have EM studies identified aging-affected structural changes in the myelin sheath of rodent WM [22,23]. Despite its capability to visualize ultrahigh resolution images, EM requires complicated sample preparation and fixation processes for limited 2D assessment of the myelin structure, and may not be suitable for efficient volumetric evaluation of ex vivo samples. In this respect, two MRI methods, QSM and R_1 , offer highly robust quantitative options to assess volumetric myelin content, bypassing the complicated sample preparation. When compared, the QSM method is known to be advantageous for its fast acquisition and simplicity, and although deemed equally promising, the R_1 measurement method requires a much longer acquisition time. However, no quantitative comparison of the accuracy between the two MRI methods is yet available. Therefore, in the current study, using MVF by TEM as the gold standard for comparison, the linearity of the relationship between MRI-derived QSM (or R_1) results and MVF was investigated to assess and determine the utility of these MRI methods in the aging study of rat CC samples collected over a wide range of ages.

In young rodents, MVF rapidly increases with age, with a sharp increase in the number of myelinated axons in the WM [20,21,36]. After this period, the aged myelinated axons became thicker and larger, but the rate of the MVF increase decreased because of the degenerative alterations of myelin, such as the splitting and decompaction of the myelin lamellae [22,23,37,38]. The results of the present ex vivo MRI and TEM studies appeared to reflect such trends as well, in which the TEM analysis confirmed that the MVF change in rat CC increased significantly (from 10% to 20%) at early stages (young to adult), while the MVF change was relatively small (from 20% to 30%) at older stages, as shown in Figure 3.5 and Table 3.1. Similarly, for QSM, there was a relatively large change in magnetic susceptibility in the early stages of development (Figure 3.5B), and R_1 also showed a large change at young ages, indicating that R_1 and magnetic susceptibility values could be used to represent MVF in the myelin evaluation of ex vivo CC (Figure 3.5).

The relationships between these two parameters and MVF are also supported by the correlation results. Between R_1 and QSM results, the mean correlation values across the quantified samples showed a significant linear relationship ($r = -0.8673$; $p < 0.01$) (Figure 3.5C). Correlation analyses of R_1 and QSM in the CC region confirmed that the trends of R_1 and magnetic susceptibility values, which change with age, are closely related. Analysis of the relationship between MVF and either R_1 or QSM, revealed that both $R_{1\text{mean}}$ ($r = 0.9138$; $p < 0.01$) and $\chi_{\text{measured,mean}}$ ($r = -0.8435$; $p < 0.01$) showed strong linear correlations with MVF (Figure 3.6B). The fact that the increase in MVF with aging is highly correlated

with the changes in R_1 and magnetic susceptibility suggests that these parameters could be quantitatively calibrated to assess myelin content. Since the QSM method is faster than R_1 acquisition and requires much less sample preparation than TEM, the significant linear relationship of magnetic susceptibility to R_1 and MVF values in aging CC suggests the usefulness of volumetric MVF monitoring using QSM.

FPM simulation using TEM data showed that MVF content in the central voxel was mainly responsible for ΔB changes in the neighboring voxels (Figure 3.8). As such, in the QSM simulation, the changes in $\chi_{\text{simulated}}$ values evaluated based on ΔB information, including neighboring voxels, reflected the increase in MVF ($r = -0.9648$; $p < 0.01$) in the CC of aging rats (Figure 3.8B). Analysis of the correlation between $\chi_{\text{simulated,mean}}$ (TEM) and $\chi_{\text{measured,mean}}$ (MRI) revealed a significant linear correlation ($r = 0.8958$; $p < 0.01$), confirming that the simulated and MRI-measured magnetic susceptibility values were consistent (Figure 3.8B). These results show that the FPM-based QSM simulation accurately reflects the volumetric effect of myelin by MRI.

Although the current FPM-based simulation considers only the isotropic susceptibility of myelin, myelin is reported to exhibit anisotropic susceptibility [33, 35]. Therefore, analytical ΔB calculations and QSM simulations for a simple hollow cylinder model were performed as complementary analyses to consider the effect of anisotropic susceptibility on MVF (Figure 3.9). Comparing the cases for (1) isotropic susceptibility alone and (2) isotropic + anisotropic susceptibilities in QSM simulations, a strong linear correlation ($r = 0.9999$; $p < 0.01$) was found between the two cases (Figure 3.9B). In addition, the simulated susceptibility (including anisotropic susceptibility in the model) decreased linearly with increasing MVF in the experimentally observed range (Figure 3.9C). Based on these results, the linear trend of our simulation results between QSM and MVF values would not change, even if the anisotropic susceptibility was considered in the QSM models; however, absolute values may need to be adjusted to facilitate a quantitative comparison with respect to MRI-derived QSM values.

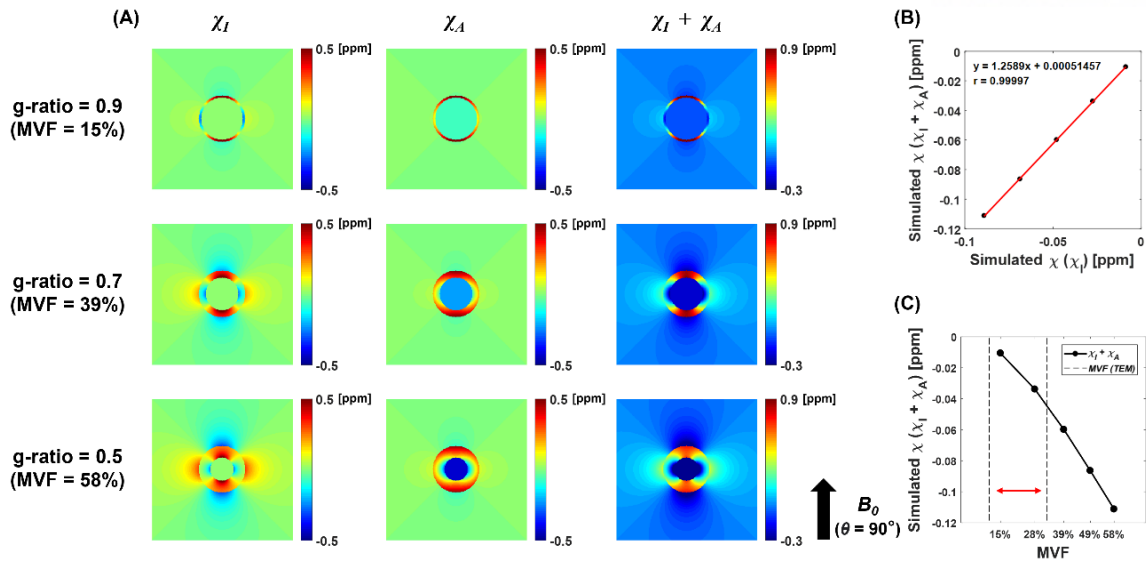


Figure 3.9. Hollow cylinder model simulation results and analyses. Simulated hollow cylinder model with different g-ratio and MVF. (A) Simulated maps of hollow cylinder model formed from a material with isotropic susceptibility (χ_I), anisotropic susceptibility (χ_A), and the sum of these values ($\chi_I + \chi_A$). These hollow cylinder models aligned perpendicular to B_0 ($\theta = 90^\circ$). (B) Scatter plot of simulated susceptibilities of χ_I and $\chi_I + \chi_A$ cases ($r = 0.9999$; $p < 0.01$) with linear fit lines. (C) Simulated susceptibilities of $\chi_I + \chi_A$ cases with MVF. The red arrow between dotted lines shows the MVF range measured by TEM.

Despite the demonstrated correlations, there were a few limitations to our study. First, the variability of the magnetic susceptibility change by diverse geometric presence of myelinated axons with respect to B_0 -orientations was not considered [17,39,40]. In this study, the orientations of myelinated axons were set perpendicular to the B_0 field to match the field variations between the simulation and experiments. However, studies considering variable orientations of perturbers may be important and can be used to assess the possible presence of directional preferences in axon development. Second, our study did not examine the longitudinal relaxation rate or magnetic susceptibility changes due to iron content [17,41]. Paramagnetic iron also accumulates as the brain ages, which could alter the longitudinal relaxation rate and offset the magnetic susceptibility values corresponding to myelin content [17,42–44]. Since the QSM algorithm we used was calculated based on the average susceptibility of the whole brain, changes such as iron accumulation that increase with age in the rest of the brain may be reflected, thus confounding the interpretation. However, the amount of iron that accumulates in CC is typically much lower (261.8 nmol/g of the CC) than in gray matter (GM) areas such as the substantia nigra (1404.0 nmol/g of the substantia nigra) [45,46]. Therefore, we hypothesized that the amount of iron did not significantly affect R_1 or QSM measurement accuracy of myelin content in the aging rat brain CC.

Additionally, considering the previously reported minor changes in iron content in aged CCs, CC is also an optimal brain region for measuring changes in R_1 and QSM values that are directly related to changes in MVF during aging [45]. However, our study has a limitation that it is applied only to the CC region, so a thorough investigation of the MR parameter changes in the additional WM regions will be of great help in quantitative evaluation of MVF. Third, *ex vivo* MRI studies must consider changes in tissue magnetic properties due to the effects of chemical fixation and temperature. In many studies, T_1 was found to have reduced values compared to *in vivo* measurements due to formalin fixation [14,17,47–49]. Temperature is considered to be a factor influencing T_1 by mediating changes in MR relaxation times that result from temperature differences between *in vivo* and *ex vivo* conditions. In the case of QSM, since magnetic susceptibility is also affected by chemical fixation and temperature, it may be difficult to accurately translate *ex vivo* MRI QSM studies [50–52], even although the contrast of post-mortem QSM within brain tissues was reported to be maintained by *in vivo* MRI [53]. Therefore, careful interpretation of the above should be considered for *in vivo* quantification of MRI T_1 and magnetic susceptibility values in myelin content estimation. Finally, the original QSM method computed ΔB through phase unwrapping from the measured MRI phases and then calculated susceptibility through field-to-source inversion, but our simulation performed QSM using ΔB information [3,32]. Along with the anisotropic susceptibility of myelin, different relaxation times between different microstructural compartments of the rat CC may induce the nonlinear accumulation of phase signals. However, these effects and molecular diffusion during MR acquisition were not included in our QSM simulation. Further rigorous simulation validations are needed to investigate the effect of the anisotropic susceptibility and the molecular diffusion in the quantitative assessment of myelin content from QSM.

In summary, our simulation and experimental studies examined the effects of myelin content, validated by TEM on MRI magnetic susceptibility and longitudinal relaxation parameters in the *ex vivo* WM samples. This was performed to validate the linear dependences of R_1 and QSM values on the absolute MVF for aging brain CC. The linear relationship between R_1 and QSM, known as an MRI-based myelin quantifying imaging method, showed that both parameters similarly reflected changes in myelin content caused by aging. The *ex vivo* MRI results and those of MVF by TEM from naturally aging CC quantitatively showed clear linear relationships between MRI parameters (R_1 and magnetic susceptibility values) and TEM-derived MVF. Utilizing FPM-based QSM simulations based on TEM data, simulated magnetic susceptibility values were found to be highly sensitive to MVF and showed a significant correlation with magnetic susceptibility values measured by MRI. These results suggest that the volumetric information of myelin obtained by MRI QSM and longitudinal relaxation rate may be considered directly as an *ex vivo* MRI surrogate for MVF in aging brain WM.

The original source of Chapter 3 is the article, Cho, H., Lee, H., Gong, Y., Kim, Y. R., Cho, J., & Cho, H. J. (2022). Quantitative susceptibility mapping and R1 measurement: Determination of the myelin volume fraction in the aging ex vivo rat corpus callosum. *NMR in Biomedicine*, 35(3), e4645.

Chapter 4. Access to the relationship between myelin volume fraction and R_2 measurement

4.1 Introduction

White matter (WM), which constitutes nearly half of the human brain, comprises millions of bundles of axons and actively influences brain learning and functioning [54]. Many axons in the WM are tightly surrounded by a lipid-protein membrane structure called myelin, which exists in the form of repetitive multilamellar layers [4,6,54]. Myelin promotes various brain functions by increasing the speed and efficiency of action potential transmission [55]. The measurements of myelin content in WM, such as myelin volume fraction (MVF), which directly affect signal conduction speed [6,54], are important for studies of normal development and neurodegenerative diseases [10,56].

Magnetic resonance imaging (MRI) has been widely used to non-invasively investigate microstructural effects, such as myelination in WM. Direct imaging of non-aqueous protons of myelin in conventional MRI is difficult because of their short T_2 ($50 \mu\text{s} < T_2 < 1 \text{ ms}$) [56]. An ultrashort echo time (UTE) sequence was developed to measure non-aqueous protons directly in the myelin, but this technique has recently been developed and limitations such as signal contamination by other macromolecules are present, requiring additional validation [57]. Therefore, quantitative MRI techniques currently used for myelin imaging are primarily based on compartmental assessment of myelin content.

Various MRI methods are being studied for quantitative analysis of myelin [10,12,58]; among these, myelin water imaging (MWI) is considered a representative method for evaluating the water components of myelin [59]. MWI is a quantitative MRI technique based on myelin water fraction (MWF) measurement, which is the fraction of MR signals from water captured in the myelin sheath bilayer [12]. The multi-echo T_2 technique is a method for measuring T_2 through signal decay curves from multiple echo times (TE) obtained by applying a 90° pulse followed by a train of 180° pulses [60,61], which is the most common method for estimating MWF [11]. In routine MWI, signals measured by the multiple spin echo sequence are separated into a short- T_2 component (myelin water; 10–40 ms from human WM) and long- T_2 component (intra- and extra-cellular (IE) water; 40–200 ms from human WM) through nonnegative least-squares (NNLS) algorithm to derive MWF [11,62]. Myelin MRI studies on humans are difficult to verify with histological counterparts, so MWI studies using animal models are being actively conducted for the direct comparative quantifications.

In rodent WM studies, several MWI studies of short- T_2 components have shown correlations between histological image analysis and MRI-derived MWF in rat sciatic nerves and spinal cords [63–65].

However, performing MWI to extract short- T_2 components in the brain WM (both in vivo and ex vivo) in rodent studies appears to be somewhat inconsistent. An in vivo rat study by Does and Gore reported that multi-echo based MR signal at 4.7T predominantly exhibited a mono-exponential T_2 relaxation in brain corpus callosum (CC) region [66]. In addition, Thiessen et al. tried to extract short- T_2 components from the CC via multiple spin echo sequences with 10 ms echo spacing in an ex vivo mouse study at 7T MRI, but no short- T_2 component was apparently found [67]. On the other hand, it was reported that the short- T_2 components from the CC were observed in ex vivo mouse studies at 7T [16], and 15.2T MRI [68]. The observed ex vivo results may be attributed to factors such as the nature of the fixative, duration of fixation and washing, which could lead to the loss of detectable (separable) short- T_2 components. Generally, chemical fixation is known to reduce T_2 in brain regions by affecting the tissue's magnetic properties, making analysis of myelin water signals difficult [48,69,70]. Currently, there is no conclusive evidence supporting the validity of ex vivo compartmental MRI- T_2 values (without separable short T_2 component) obtained through conventional fixation methods as an alternative means of measuring MVF in the WM of the rat brain.

The main objective of this study is to determine whether myelin volume information can be detected even when short- T_2 component is undetectable due to effect such as fixation in post-mortem brain. This study evaluates age-related myelin changes in post-mortem rat CCs through a conventional simple fixation method without prolonged washout. First, multiple spin echo sequence-based signals were obtained through MRI experiments on each age group, and then the obtained signals were analyzed through mono- and multi-exponential relaxation fitting processes. In this study, R_2 (the reciprocal of T_2) values derived through the fitting processes were used under the assumption that there was a linear and positive correlation with the age-related myelin volumetric changes. After MRI experiments, transmission electron microscopy (TEM) processing was performed to directly evaluate the myelin content as histological verification. Thereafter, as a theoretical verification step, relaxation rate by diffusion of protons ($R_{2,IE}$) in the presence of susceptibility induced magnetic field variations due to myelin were calculated from each TEM image to verify the susceptibility effect of myelin in IE water signals. The relationship between MRI- R_2 values and TEM-derived myelin contents in aging ex vivo rat CC was derived and rationalized by correlating the mono- and multi-exponential relaxation fitting results of the multiple spinecho sequence-based R_2 measurement, TEM-derived myelin volume fraction (MVF) parameter, and simulated susceptibility effects of IE water ($R_{2,IE}$).

4.2 Methods

4.2.1 Animal preparations

All experimental procedures were performed with the approval of the Institutional Animal Care and Use Committees (IACUC) of the Ulsan National Institute of Science and Technology (UNISTIACUC-19-01). Three groups of female Sprague-Dawley rats ($n=9$) of different ages were used: Young, Adult, and Old groups. 6-week-old rats were selected as a Young ($n = 3$) and purchased from Orient Bio (Gyeonggi, Republic of Korea). Adult ($n = 3$) and Old ($n = 3$) consisted of 4- and 20-month-old rats, respectively, and were purchased from the Aging Tissue Bank (Pusan National University, Republic of Korea). To obtain clearly fixed brains, intracardiac perfusion with saline and 10 % neutral buffered formalin was performed in anesthetized rats. Subsequently, the brains were extracted while preserving the skull so as not to directly damage the brain, and after removing all external tissues of the skull, the brains (in skull) were post-fixed in 10 % neutral buffered formalin. This fixation process was performed over 6 and a half months in the all group until the fluctuations in MRI values due to fixation were sufficiently stable (at least 5 months) [71]. The sufficiently fixed samples were sealed in formalin-filled 30 mL syringes and used for MRI experiments at room temperature [72].

4.2.2 MRI acquisition and analyses

MRI data were obtained using a 40 mm volume coil on a 7T animal MRI scanner (7.0T Bruker PharmaScan; Bruker Biospin, Ettlingen, Germany). The multi-echo spin-echo sequence acquisition was run with repetition time (TR) = 4000 ms, TE = 8–384 ms (echo images = 48, echo spacing = 8 ms), field of view = $25 \times 25 \text{ mm}^2$; matrix size = 256×256 ; slice thickness = 0.4 mm; number of slices = 1; and number of averages (NA) = 4 (total scan time: 1 h 8 min). For all samples, a slice position located at -6 mm from bregma was used, which was estimated based on the skull of each sample and assisted by the Rat Brain Atlas [73]. Here, gradient spoilers were applied before each excitation RF pulse to minimize previous signals and also applied on both sides of the refocusing RF pulses to minimize unwanted coherences. In all samples, the angle between the axons of the CC region and the main magnetic field was positioned to be perpendicular based on information from the Diffusion Tensor Imaging Atlas of the Rat Brain [74].

All MRI data analyses were performed using MATLAB R2022a (The MathWorks, Inc., Natick, Massachusetts, USA), and the CC, the largest WM region in the brain [29], was manually segmented and used as a region of interest (ROI).

Quantitative MRI-measured R_2 values for each pixel were calculated by nonlinear least-square curve fitting as a mono-exponential relaxation equation ($S(TE) = S_0 e^{-TE R_2} + S_{offset}$), where S_0 is the amplitude of signal at TE = 0 and S_{offset} is a baseline constant used to minimize the fitting and represents a non-

zero baseline for considering signals that may not converge to zero [75,76]. In addition to R_2 , S_0 and S_{offset} values are also fitted for each pixel. ROI averages of R_2 over pixels for each age group were used for mono-exponential relaxation data analysis.

A multi-exponential relaxation fitting process was additionally applied to confirm that the short- T_2 components were detected. Here, this signal is assumed to be a multi-exponential relaxation signal, and expressed in a general equation ($S(TE) = \sum_{j=1}^M S_j e^{-TE/T_{2j}} + S_{offset}$), where S_j is the relative amplitude corresponding to each relaxation time component T_{2j} , and M is the number of logarithmically spaced T_{2j} components. Based on this equation, multi-exponential relaxation fitting was implemented with a NNLS algorithm for T_2 values logarithmically spaced between 4 ms and 500 ms ($M = 200$), and minimum curvature regularization was also performed to smooth the resulting T_2 spectrum (regularization parameter $\mu = 0.002$) [62, 77]. For the signal amplitude used in this process, the average values of the pixels in the ROI were used, and the average of non-zero T_2 values of the resulting T_2 spectrum for each sample was derived as $T_{2,Multi}$ (the reciprocal: $R_{2,Multi}$). This set of analyses was performed using the freely available multi-exponential relaxation analysis (MERA) toolbox for MATLAB [78]. Also, in each fitting process (both mono- and multi-), the R-squared (R^2 ; the coefficient of determination) value that measures each goodness-of-fit is calculated and used for fitting evaluation.

As an additional study, it was investigated whether short- T_2 and long- T_2 components could be separated from T_2 spectra obtained through multi-exponential fitting through a single threshold across different age groups by setting a T_2 -cutoff value. The MWF of each spectrum is calculated as the ratio of signals with T_2 lower than the T_2 -cutoff value to the total signals in the T_2 spectrum, and the T_2 -cutoff value was set to the best match between the MVF and MWF values for each sample. Here, one of the 6-week-old and 20-month-old samples was selected and analyzed how the MWF value changes according to each T_2 -cutoff value.

4.2.3 Microscopy

Each sample was processed for histological verification by TEM as follows: extraction of CC from the same slice location used for MRI (-6 mm from bregma), sectioning the upper left corner of CC to make a 1 mm³ tissue block, fixation of the tissue block in 1 % osmium tetroxide in a phosphate buffer, dehydration through ethanol and propylene oxide, and curing in Eponate 12 resin (Ted Pella Inc., Redding, USA). Fully cured tissue blocks were cut into ultrathin sections (100 nm) perpendicular to the axis of the WM fibers by an ultramicrotome (EM UC7, Leica). Ultrathin sections were then examined using TEM (Tecnai G2 F20 X-Twin, FEI) operated at 200 kV, collecting 3–7 images per sample consecutively with a magnification factor of 2,300. 60–150 myelinated axons were measured for each image, and at least 200–300 myelinated axons were measured for each sample. These TEM processes

have been described in detail in a previous study [72]. Subsequently, 2D TEM images were manually segmented into three compartments (intra-cellular space, myelin, and extra-cellular space) using GIMP (<https://www.gimp.org/>). In this process, each axon was classified individually, making it possible to measure the myelin sheath thickness (MST) of each axon. The MVF value was calculated as the proportion of pixels corresponding to the myelin region among the total pixels of the segmented TEM image, using MATLAB. The mean MST value of each TEM image was calculated by the sphere fitting method using BoneJ [79–81], and image analysis plugin in ImageJ [82]. These processes are described in Figure 4.1.

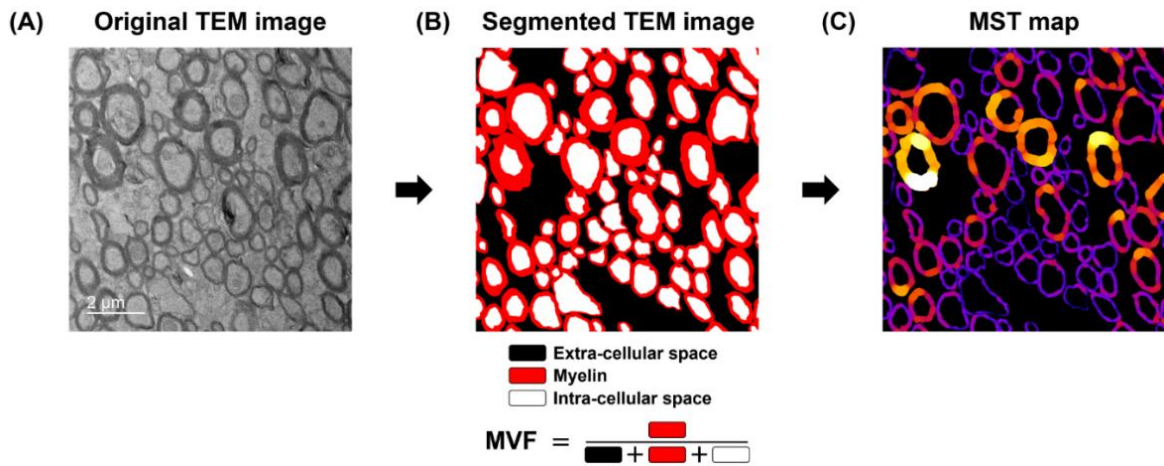


Figure 4.1. Brief description of how to calculate TEM-derived parameters (MVF and MST) from TEM image. Representative (A) TEM image and (B) segmented image (scale bar = 2 μm). In the segmented TEM image, each color-coded rectangle (black, red, and white) indicates the area of the corresponding compartment, and MVF is calculated through these areas. (C) Graphical MST map of TEM image. Thicker the MST of the axon, brighter the color.

4.2.4 Simulation part 1: field perturbation mapping

The field perturbation-dependent components of multiple spin echo sequence-based MRI- T_2 can be considered as follows [83,84]:

$$\frac{1}{T_2} = \frac{1}{T_{2,0}} + \frac{1}{T_{2,D}} \quad (1)$$

where $T_{2,0}$ is the inherent relaxation due to spin-spin interactions, and $T_{2,D}$ is the relaxation due to diffusion of protons in the field perturbation map. This Eq. (1) states that the diffusion of water protons during the presence of field perturbation due to myelin may affect the multiple spin echo signal. When analyzing the effect of $T_{2,D}$, the diffusion in the myelin area is insignificant compared to other compartments [65], so the main diffusion area is regarded as the IE spaces and $T_{2,D}$ can be expressed as

$T_{2,IE}$ (the reciprocal: $R_{2,IE}$). In this part, using the TEM data, TEM-based simulations were performed to investigate how multiple spin echo sequence-based signals were affected by diffusing water protons in the presence of inhomogeneous magnetic field due to susceptibility difference between myelin and underlying brain tissues in IE spaces.

The simulation process consists of a generation part of the field perturbation map generated by the myelin structures, and a computational part of the multiple spin echo sequence-based signal generated by diffusing protons in the presence of generated local field perturbations. Three-compartment segmented 2D TEM images (matrix size = 2048×2048 pixels with resolution = $0.0047 \mu\text{m}$), which were used for MVF and MST calculations, were used as realistic geometric models for simulations. In these simulations, the myelinated axons were assumed to be infinitely hollow cylinders along the longitudinal direction.

The first step in the field perturbation mapping part was to define the magnetic susceptibility of the pixels. For myelin, magnetic susceptibility anisotropy due to the orientation of the myelin phospholipids must be considered for accurate simulation [77–79]. Thus, total magnetic susceptibility of myelin X takes the form of a rank 2 tensor, expressed as the sum of the isotropic (X_i , where tensor parts $\chi_{\parallel} = \chi_{\perp}$) and anisotropic susceptibility components (X_a , where tensor parts $\chi_{\parallel} \neq \chi_{\perp}$) as follows [35,85–87]:

$$X = X_i + X_a = \begin{bmatrix} \chi_i & 0 & 0 \\ 0 & \chi_i & 0 \\ 0 & 0 & \chi_i \end{bmatrix} + \begin{bmatrix} \chi_a & 0 & 0 \\ 0 & -\frac{\chi_a}{2} & 0 \\ 0 & 0 & -\frac{\chi_a}{2} \end{bmatrix} \quad (2)$$

where χ_i and χ_a denote the isotropic and anisotropic magnetic susceptibility constants of myelin, respectively. In this study, χ_i and χ_a of myelin were set to -0.13 ppm and -0.15 ppm, which were determined by reference to several literatures [33,35,87,88]. The magnetic susceptibilities of IE spaces were set to zero. After that, susceptibility tensor is expressed as a common reference frame of the axon X_R , computed as follows [35,87,88]:

$$X_R = R_z(\phi) X R_z^T(\phi) \quad (3)$$

where $R_z(\phi)$ is the rotation matrix and ϕ is the angle between phospholipids and the magnetic field B_0 . Phospholipid orientation of each axon is calculated by smoothing through a Gaussian filter to generate the gradient from extra- to intra-cellular space, a detailed process for which is described by Hédouin et al. [88]. Using the susceptibility tensor map X_R calculated in the previous step, field perturbation map ΔB in the frequency domain is calculated as described in Li et al. [89]. Calculation of the 2D field perturbation map assumed that the geometries of the axons were constant in 3D, and the orientation of axons was fixed perpendicular to the magnetic field. In this process, the magnetic field strength was fixed at 7T as in the MRI experiment.

4.2.5 Simulation part 2: Signal decay in IE spaces due to field perturbations

To simulate the relaxation rate due to diffusion in the presence of inhomogeneous magnetic field in IE spaces ($R_{2,IE}$), the diffusion effect of the protons is added so that the phase accumulation by random diffusion is applied at each time-step. Protons are randomly distributed and diffused through a Monte-Carlo approach in the presence of TEM-derived field perturbation map. In this Monte-Carlo diffusion model, it is assumed that the myelin region is impermeable so that protons can only diffuse within each initially randomly assigned compartment (IE spaces and myelin). In addition, it is assumed that diffusion of protons in myelin region is neglected because diffusion in myelin region is very negligible compared to other compartments [65]. These settings were established to see how protons in the inhomogeneous magnetic field affect the signal, excluding effects such as water exchange between compartments in MRI- R_2 measurements. Detailed mechanisms of how protons are moved by diffusion coefficient and time-step are described in Pathak et al. [31]. The total phase φ accumulating due to the diffusion of protons is calculated as follows [31]:

$$\varphi_n(t) = \sum_{j=1}^{\lceil t/\Delta t \rceil} 2\pi \Delta B(p_n(j\Delta t)) \Delta t \quad (4)$$

where Δt is the diffusion time-step and p_n is the position of n^{th} proton through time t . As protons diffuse, the accumulated phase periodically refocused from 180° pulses, and signals are extracted based on the accumulated phase information for each TE. The simulated multiple spin echo sequence-based signal due to the diffusion effect is calculated as follows [31]:

$$S(t) = \frac{1}{N} \sum_{n=1}^N e^{i\varphi_n(t)} \quad (5)$$

where N is the number of protons through time t . Using the extracted signal for each TE, simulated $R_{2,IE}$ values by diffusion of protons for each TEM image were calculated by nonlinear least-square curve fitting. The parameters related to diffusion used in simulation were as follows : number of protons = 50,000; TE = 8–104 ms (echo images = 13, echo spacing = 8 ms); Δt = 0.02 ms; apparent diffusion coefficient (ADC) = $2 \mu\text{m}^2/\text{ms}$ [90]; and NA = 2. Here, the range of TE is a value obtained through experiments, and is set as the time taken until all signals to reach the baseline.

4.3 Results

Representative MRI positioning and ex vivo MRI- R_2 maps for each age group are shown in Figure 4.2. The location of the slice used for the MRI experiment is illustrated in Figure 4.2A. The CC regions of each sample used as ROIs are marked in white in Figure 4.2B. In the mono-exponential relaxation fitting case, an increase in R_2 values due to aging within CC was evident (Figure 4.2B). The rate of change of R_2 was 15.71 % in the early developmental stage (6-week to 4-month; 32.3241 s^{-1} to 37.4027 s^{-1}) and 4.59 % in the aging stage (4-month to 20-month; 37.4027 s^{-1} to 39.1204 s^{-1}), suggesting that the

increase in R_2 is larger in the early developmental stage (Table 4.1). Almost all R^2 values were higher than 0.9, indicating that the mono-exponential relaxation fitting process was performed adequately (Figure 4.3).

Methods		6-week	4-month	20-month
MRI	R_2 [s^{-1}]	32.3241 (± 2.5706)	37.4027 (± 2.9287)	39.1204 (± 2.9304)
	$R_{2,Multi}$ [s^{-1}]	32.2711 (± 2.7720)	37.1795 (± 3.1248)	39.2147 (± 3.4212)
Simulation	$R_{2,IE}$ [s^{-1}]	0.1100 (± 0.0430)	0.1447 (± 0.0575)	0.2102 (± 0.0588)
TEM	Number of TEM slice	14	14	14
	Mean MVF [fraction]	0.1270 (± 0.0292)	0.2112 (± 0.0516)	0.2907 (± 0.0387)
	Mean MST [μm] (S.E.)	0.0994 (± 0.0026)	0.1072 (± 0.0077)	0.1460 (± 0.0079)

Table 4.1. MRI and TEM data analysis results of age groups. It is presented as the mean and standard deviation (or standard error; S.E.) of all values belonging to the same age group.

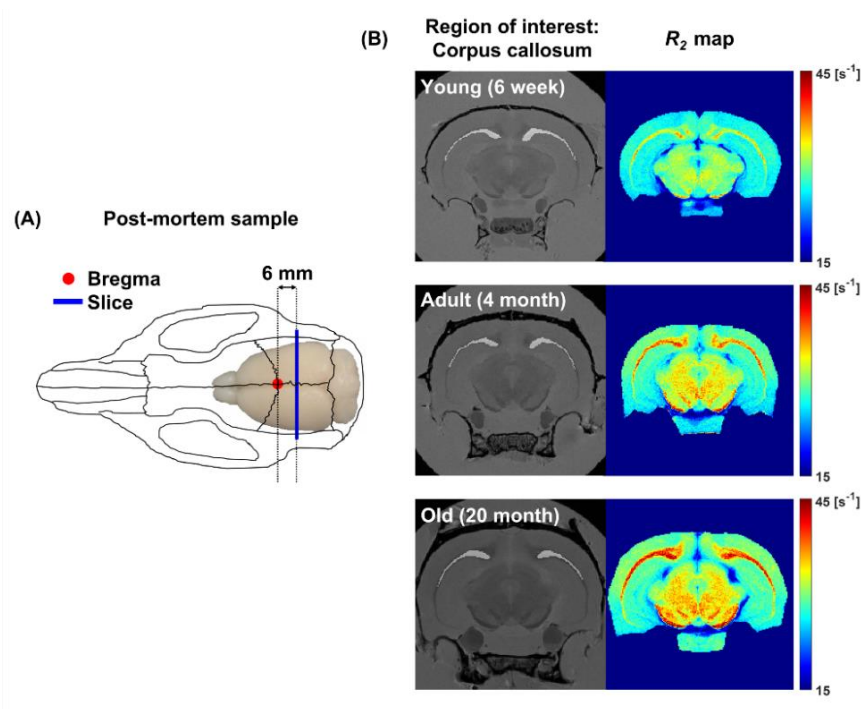


Figure 4.2. The representative ex vivo MRI positioning and results. (A) Schematic illustration of MRI slice positioning in post-mortem sample: rat brain with skull. A coronal slice (marked in blue-line) is

placed -6 mm from bregma (marked in red-dot). (B) The regions of interest showing the corpus callosum region (marked in white) in proton density-weighted images (left) and R_2 maps (right) calculated by mono-exponential relaxation function of each age group (Young: 6-week-1, Adult: 4-month-1, and Old: 20-month-2).

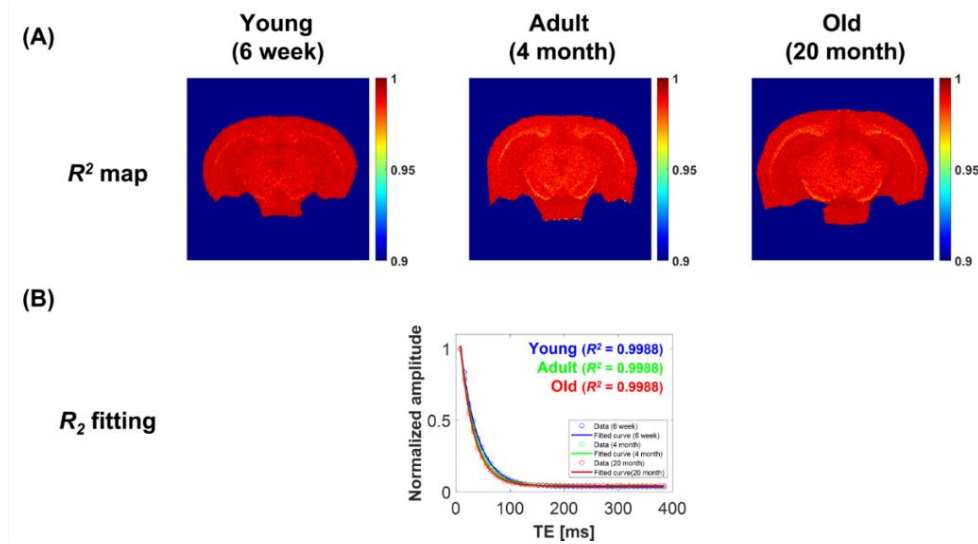


Figure 4.3. Mono-exponential fitting qualities. (A) Representative R -squared (R^2 ; the coefficient of determination) maps and (B) mono-exponential fitted curves with the mean signal of the CC region of each age group (Young: 6-week-1, Adult: 4-month-1, and Old: 20-month-2). R^2 values for each age group are color-coded (Young: blue, Adult: green, Old: red).

Representative multi-exponential relaxation fitting results with the mean signal of the CC region pixels of each age group are shown in Figure 4.4. Similar to the mono-exponential relaxation fitting results shown above, almost all R^2 values were higher than 0.9 (Figures. 4.4A-4.4C), and it was confirmed that $R_{2,Multi}$ values increased with age (Figure 4.4D). However, it was observed that the representative T_2 spectra of each group were not clearly separable into short- T_2 components and long- T_2 components (Figure 4.4D).

In order to confirm that the short- T_2 components did not exist or were detected but mixed with long- T_2 components and were not distinguished, myelin changes in actual samples were confirmed through verification processes: TEM analysis and TEM-based simulation. An illustrative TEM processing procedure is described in Figure 4.5. Representative TEM and segmented images of each age group are shown in Figure 4.6A. It can be clearly observed from the segmented images that MVF and MST increased with age (Figure 4.6A). In Figure 4.6B, a polynomial fitting curve is used instead of a linear fit line to show the detailed relationship between the MVF and MST for each TEM image. Through this fitted curve, it was observed that MVF increased with age, but the rate of change of MST in the early

developmental stage was 7.85 % (0.0994 μm to 0.1072 μm), which was almost unchanged compared to MVF (Figure 4.6B). In addition, the rate of change in MVF at the aging stage was 37.64 % (0.2112 to 0.2907 [fraction]), which was much smaller than 66.30 % in the early stage of development (0.1270 to 0.2112 [fraction]), as shown in Figure 4.6B. Detailed MRI- and TEM-based values are summarized in Tables 4.1 and 4.2.

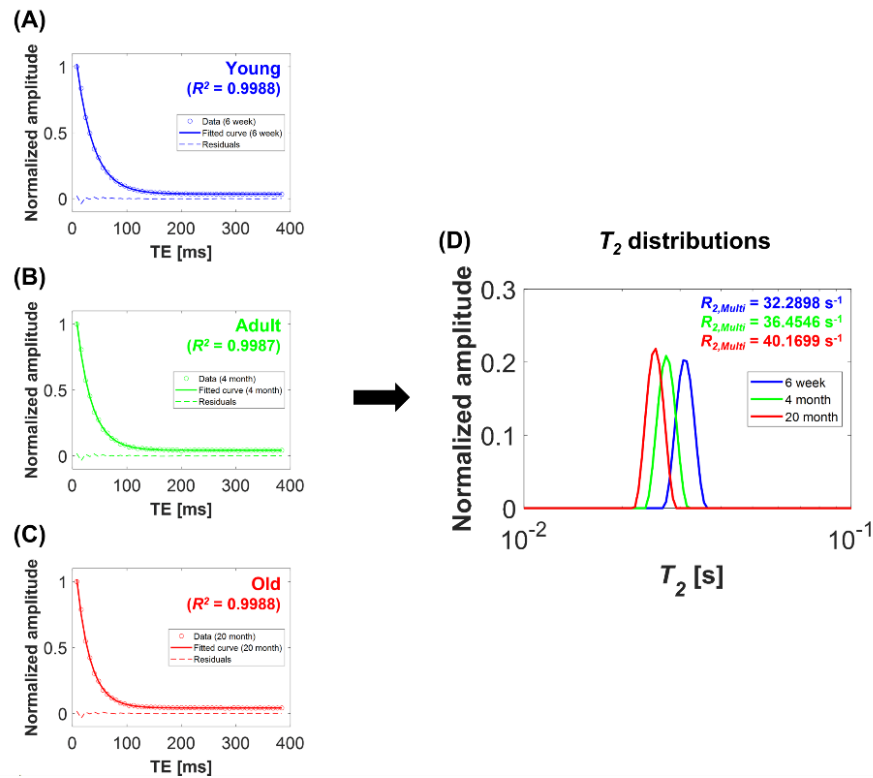


Figure 4.4. Multi-exponential relaxation fitting results. (A-C) Representative T_2 decay and fitted curves with the mean signal of the CC region of each age group (Young: 6-week-1, Adult: 4-month-1, and Old: 20-month-2). (D) T_2 distributions derived from the fitted curves in (A-C). R_2 and $R_{2,Multi}$ values for each age group are color-coded (Young: blue, Adult: green, Old: red).

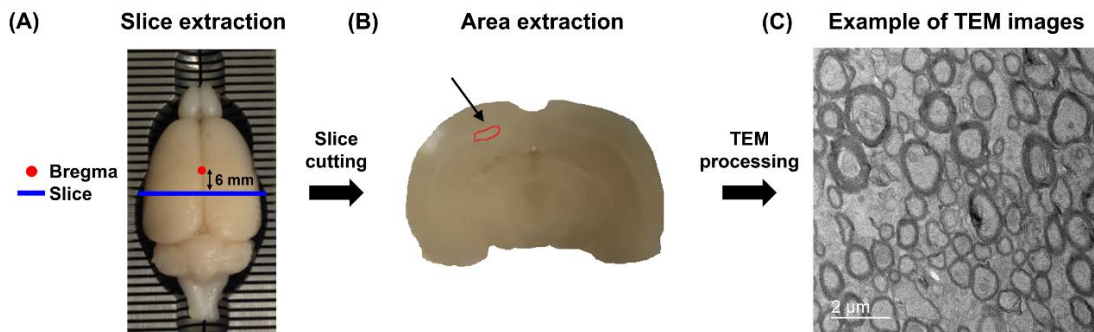


Figure 4.5. Histological verification process by TEM. (A) Brain slice extraction from the same location (marked in blue-line) as the slice used for MRI (-6 mm from bregma marked in red-dot). (B) Cut the

upper left corner of the corpus callosum region (marked in red) to be used for TEM processing. (C)
 Example of resulting image after TEM processing.

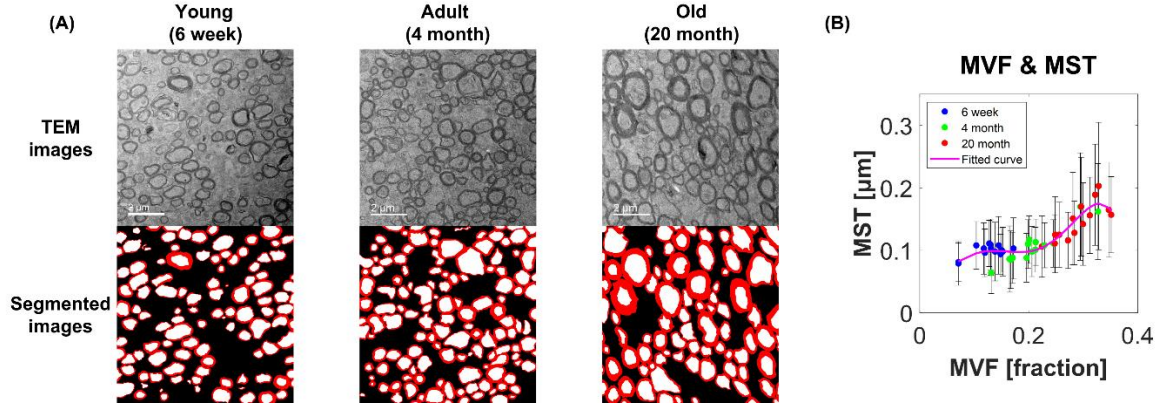


Figure 4.6. The representative TEM images and correlation between each TEM-derived parameter. (A) TEM and segmented images of each age group (Young: 6-week-1, Adult: 4-month-1, and Old: 20-month-2; scale bar = 2 μm). (B) Scatterplot of MVF and mean MST of each TEM image with 5th-degree polynomial fitted curve.

Methods		6-week-1	6-week-2	6-week-3	4-month-1	4-month-2	4-month-3	20-month-1	20-month-2	20-month-3
MRI	R_2 [s^{-1}]	32.4703 (± 2.6745)	31.9578 (± 2.4838)	32.6090 (± 2.5025)	36.9038 (± 3.0477)	37.6086 (± 3.0798)	37.6849 (± 2.5371)	38.2794 (± 2.8711)	39.8998 (± 2.8197)	39.0826 (± 2.8840)
	$R_{2,Multi}$ [s^{-1}]	32.2898 (± 2.8227)	31.9200 (± 3.0135)	32.6655 (± 2.6270)	36.4546 (± 3.1867)	37.3499 (± 3.2650)	37.7845 (± 3.0387)	38.2672 (± 3.3452)	40.1699 (± 3.5115)	39.2070 (± 3.4274)
Simulation	$R_{2,IE}$ [s^{-1}]	0.1411 (± 0.0351)	0.0678 (± 0.0297)	0.0873 (± 0.0156)	0.1947 (± 0.0298)	0.0823 (± 0.0281)	0.1039 (± 0.0089)	0.1512 (± 0.0110)	0.2551 (± 0.0458)	0.1839 (± 0.0303)
TEM	Number of TEM slice	7	3	4	7	3	4	4	7	3
	Mean MVF [fraction]	0.1463 (± 0.0164)	0.1106 (± 0.0343)	0.1055 (± 0.0251)	0.2440 (± 0.0494)	0.1544 (± 0.0201)	0.1963 (± 0.0183)	0.2569 (± 0.0266)	0.3201 (± 0.0251)	0.2669 (± 0.0256)
	Mean MST [μm] (S.E.)	0.1006 (± 0.0017)	0.0970 (± 0.0092)	0.0990 (± 0.0068)	0.1273 (± 0.0101)	0.0783 (± 0.0072)	0.0938 (± 0.0034)	0.1152 (± 0.0047)	0.1661 (± 0.0083)	0.1400 (± 0.0150)

Table 4.2. Detailed MRI and TEM data analysis results of all samples (S.E. : standard error).

In the TEM-based simulation part, magnetic susceptibility anisotropy of myelin phospholipids was applied using a hollow cylinder model (Figure 4.7A). Phospholipid orientation ϕ map and calculated field perturbation maps of single myelinated axon are shown in Figure 4.7B. Field perturbation maps

for each TEM image generated via the above mechanism are used to calculate the $R_{2,IE}$ term. An example of schematic diagram of a periodically repeated 180° refocus pulse and signal calculated at each TE in a multiple spin echo simulation is shown in Figure 4.7C. $R_{2,IE}$ values are calculated by fitting the extracted signal for each TE. An example of proton diffusion trajectories during 0 to 2 ms is shown in Figure 4.7C. In this part, representative six protons were assigned to myelin and IE spaces to clearly reveal the diffusion trajectories in IE spaces during the simulations. Here, as mentioned in the Methods section, the diffusion of protons does not cross over to other compartments and protons in the myelin region do not diffuse (Figure 4.7C).

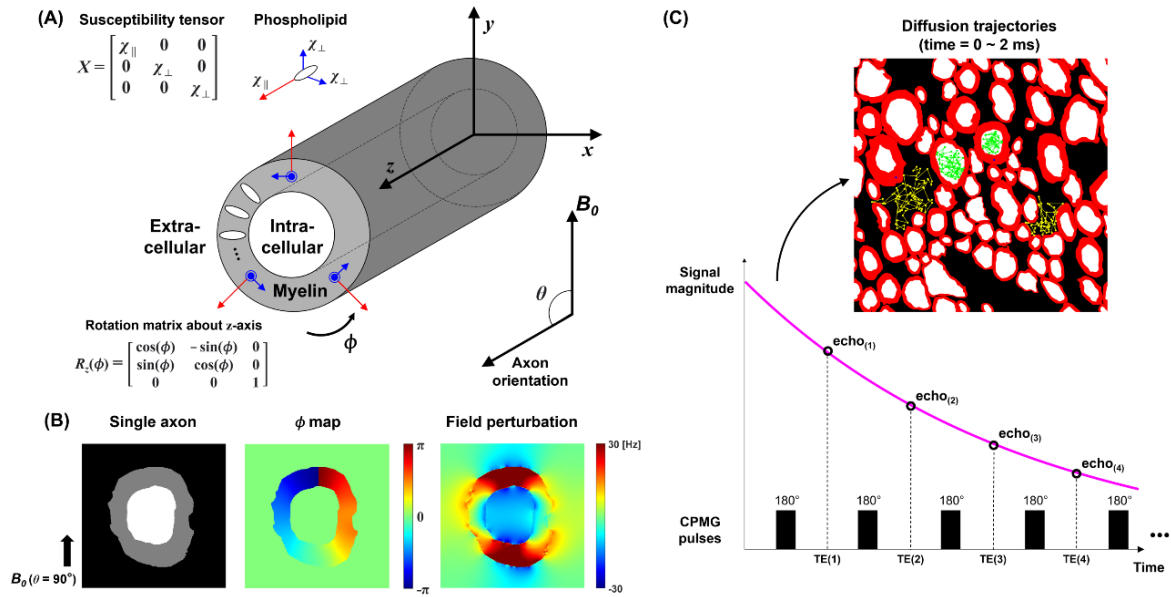


Figure 4.7. Schematic of the susceptibility anisotropy and diffusion of protons in simulation. (A) Magnetic susceptibility anisotropy of myelinated axons depicted with a hollow cylinder model. (B) A segmented single axon image (left), ϕ map of this axon (center), and field perturbation map for “ $\chi_i = -0.13$ ppm, $\chi_a = -0.15$ ppm, and $\theta = 90^\circ$ ” (right) computed in the same axon model and B_0 direction. (C) Schematic of simulated multiple spin echo pulse sequence with signal magnitude curve (magenta) and example of accumulated proton diffusion trajectories from time = 0 to 2 ms in segmented TEM image. Each proton ($n = 6$) is shown in yellow (extra-cellular space), blue (myelin), and green (intra-cellular space) depending on its assigned region.

Comparisons between R_2 , $R_{2,Multi}$, and $R_{2,IE}$ values were shown with respect to TEM-derived MVF (Figure 4.8). Through the MVF information obtained through TEM processing, it was shown that both R_2 and $R_{2,Multi}$ values obtained by the multiple spin echo sequence-based MRI experiment were proportional to the myelin content (Pearson’s correlation coefficient $r = 0.8763$ and 0.8785 ; $p < 0.01$),

suggesting that the myelin water signal influenced our MRI experiment (Figures 4.8A and 4.8B). Estimated $R_{2,IE}$ values from Monte-Carlo simulations in IE water signals were also positively correlated ($r = 0.8281$; $p < 0.01$) with MVF values, but the range of $R_{2,IE}$ values were much smaller than MRI- R_2 values (Figure 4.8C). These results indicate that changes in MRI- R_2 related MVF are likely dominated by myelin water content, as $R_{2,IE}$ cannot fully explain the observed MRI- R_2 changes.

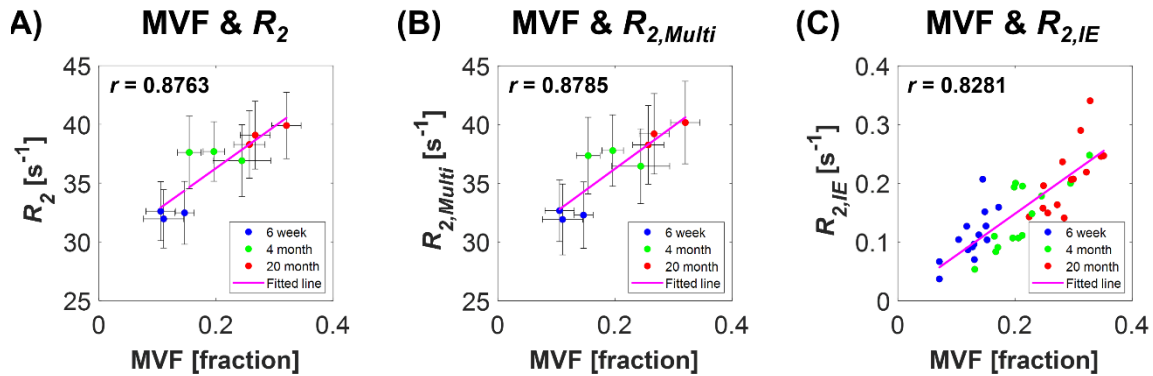


Figure 4.8. Correlation analyses between parameters for each experiment: MRI, TEM, and simulation. Scatterplots of mean MVF and other parameters : (A) R_2 (Pearson’s correlation coefficient $r = 0.8763$; $p < 0.01$). Region of interest (ROI) averages (mean and standard deviation) of R_2 over pixels for each age group were used. (B) $R_{2,Multi}$ ($r = 0.8785$; $p < 0.01$), and (C) simulated $R_{2,IE}$ ($r = 0.8281$; $p < 0.01$) with linear fitted lines.

Finally, we investigated whether it would be possible to separate the short- and long- T_2 components in the T_2 spectrum by a single threshold across different age groups by setting a T_2 -cutoff value. When the T_2 -cutoff value of the samples representing each group was adjusted to the MVF of the 20-month-old sample, it was confirmed that there was no agreement at all in the 6-week-old sample (Figure 4.9A), and the same phenomenon appeared in the opposite case (Figure 4.9B). Thus, no single T_2 -cutoff value could be obtained to estimate the proportions of the short- T_2 and the long- T_2 components across different age groups.

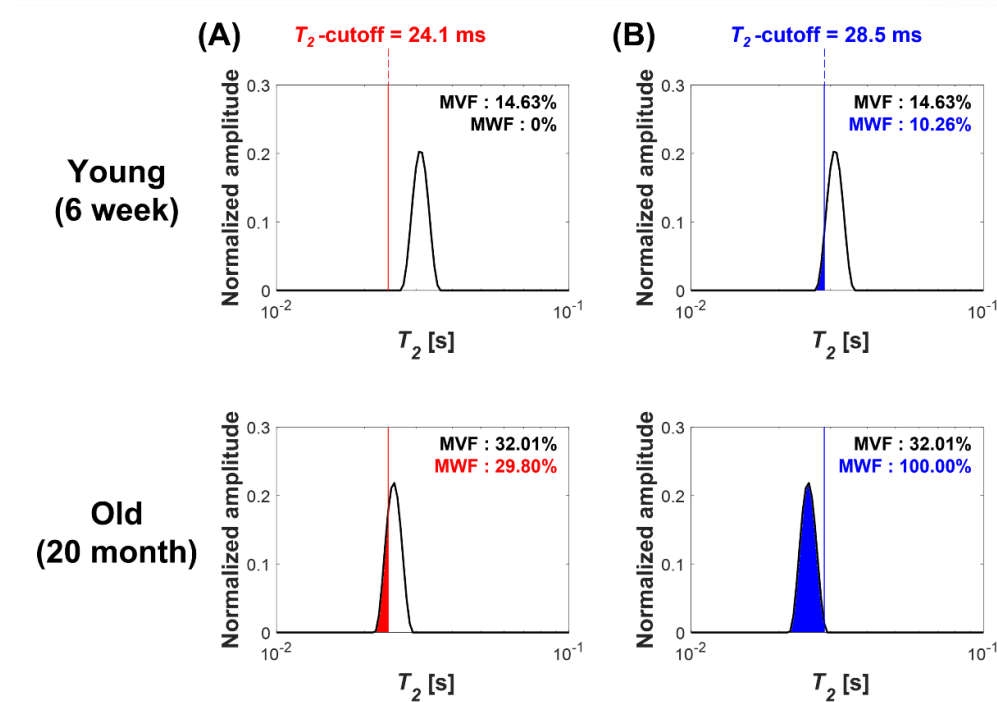


Figure 4.9. Separation of the representative T_2 distributions by different T_2 -cutoff values. Changes in myelin water fraction (MWF) in representative T_2 distributions of different age groups (6-week-1 and 20-month-2) at different T_2 -cutoff values that make the myelin volume fraction (MVF) and MWF of the sample as equal as possible. (A) T_2 -cutoff value = 24.1 ms (based on the MVF of Old sample) and (B) T_2 -cutoff value = 28.5 ms (based on the MVF of Young sample).

4.4 Discussion and Conclusions

4.4.1 Age related changes in myelin

In this study, changes in myelin content due to aging in rat brain WM were investigated using MRI, and the results were compared with respect to TEM-based myelin information and associated simulations. Thus, it is important to note the representability of current specimens for monitoring age-related myelin changes. Aging-induced changes in WM myelin in the rat brain can be classified into two major stages: early development and aging. Several previous studies confirmed that the number of myelinated axons increases rapidly, but the diameter of the axons changes little during development in the WM of young rodents [20,21,36]. In older rodents, myelinated axons thicken and increase in size [22,38], and that age-related demyelination gradually reduces the increasing trend of MVF with age [23,37]. In our TEM analysis, similar to the results of previous studies, MVF was observed to increase, but MST hardly changed in the early developmental stage; the rates of change in MVF decreased (66.30% to 37.64%) and MST increased (7.85% to 36.19%) during the aging stage (Figure 4.6B). These similarities of our TEM analysis results with those of previous histological studies indicate that the WM

samples and corresponding TEM images used in this study are representative of aging rodent myelin investigations.

4.4.2 Interpretation of multi-exponential relaxation fitting

It was found that the results of multi-exponential relaxation fitting revealed a single peak in all T_2 distribution results across different age groups. (Figure 4.4). It is important to verify whether the cause of these results is actually a reduced myelin water fraction in the post-mortem (formalin-fixed) rat CC region or a change in myelin water MRI signal through several comparative analyses. In the experiments performed, a significant increase in the value of R_2 was observed with increasing myelin content, suggesting the possibility that the myelin water signal was mixed and influenced the IE water signal of the multiple spin echo sequences (Figures 4.8A and 4.8B). Comparing our results to various previously mentioned *ex vivo* mouse studies, Thiessen et al reported a poor correlation between myelin content and mono-exponential T_2 by not detecting the short- T_2 component [67]. Additionally, other studies detected the short- T_2 component and found a good correlation with myelin content [16,68]. Therefore, it is important to discuss the experimental differences that led to these different results.

To explain these experimental results, two main factors can be considered: chemical fixation and water exchange between compartments. In conducting post-mortem MRI, various factors such as the choice of fixative types, fixation and washing time, sample size, and temperature may have a significant influence in the chemical fixation process, so experimental parameters should be selected carefully [91]. Thiessen et al. processed post-mortem mouse brains using the following procedure: intracardial perfusion with phosphate buffered saline (PBS) for ~ 2 min followed by 0.5 % glutaraldehyde (GA) and 2 % paraformaldehyde (PFA) for ~ 10 min, wash the remaining fixative with PBS, store the brain in PBS with the skull, and conduct MRI experiments at room temperature within the fomblin [67]. In this study, it was confirmed that the short- T_2 component was not detected in post-mortem mouse brain through this procedure. For other studies, Soustelle et al. processed post-mortem mouse brains using the following procedure: transcatheter perfusion with 4 % PFA for ~ 10 min, precede by heparinized physiological serum, wash the remaining fixative with PBS for ~ 10 min, store the brain at 4 °C in PBS for at least 15 days, and conduct MRI experiments at room temperature within the perfluoropolyether [16]. West et al. processed post-mortem mouse brains using the following procedure: perfusion with PBS and 2.5 % GA and 2 % PFA, store the brain in the same fixative for 1 week, wash the remaining fixative with PBS and 0.01 % sodium azide (4-5 times for 1 week), and conduct MRI experiments at room temperature within the fomblin [68]. In these studies, it was confirmed that the short- T_2 component was detected in post-mortem mouse brain through their respective procedures.

The *ex vivo* mouse studies mentioned above used varying concentrations of fixative and fixation and washing times. Therefore, even if there were changes in the experimental results due to fixation issues, it is difficult to pinpoint the exact causes [16,62,68]. Therefore, in our experiment, chemical fixation was performed using the 10 % neutral buffered formalin, which is used as the most common fixative [92,93], and water component detection was attempted through a very simple fixation process without additional washing processes. For studies using 10 % neutral buffered formalin, several human studies have confirmed little change in myelin water signal in brain WM [15,94]. These studies showed a strong correlation between stained myelin content obtained using luxol fast blue (myelin staining) and MWF in formalin-fixed human brains. Additionally, Laule et al. found that formalin fixation in human brain affected and decreased the long- T_2 components, whereas the short- T_2 components were relatively unchanged [15]. In the *ex vivo* rat study, it was confirmed that both short- T_2 and long- T_2 components of the spinal cord were shortened compared to *in vivo*, but the change in short- T_2 component was relatively small [64]. To the best of our knowledge, we did not find any studies related to this in post-mortem rat brain WM studies, but these findings support the hypothesis that our T_2 distribution results can be a mixture of reduced long- T_2 components and relatively unchanged short- T_2 components by formalin fixation (Figure 4.4).

However, recently published post-mortem human studies confirmed that fixation with 10% formalin can significantly affect myelin water signal [49,95]. Therefore, it is necessary to pay more attention to the assumptions mentioned above, and water exchange effect, another major factor that can affect the experimental value, may be an important cause for the observed correlation between R_2 and MWF values. Water exchange between myelin and other compartments can be also considered a factor that can affect myelin water signal measurements. Several rodent spine studies have reported an underestimation of MWF values due to water exchange effect [65,96]. This effect is known to increase as MST becomes thinner in myelinated axons, and fixation by formaldehyde is also known to increase the water exchange effect and consequently decrease T_2 [65,70,96]. Based on the characteristics mentioned above, even in our experiments using an aged rat model in which the MST becomes progressively thicker (Figure 4.6), it can be speculated that the enhanced exchange of water between myelin and IE spaces resulted in a decrease in T_2 relaxation time of IE water in proportion to MWF.

4.4.3 Effect of magnetic susceptibility variations in WM

After assessing how the IE water signal affects the R_2 value obtained from the magnetic susceptibility-induced field perturbation map using a multiple spin echo sequence, it was found that the proportionality trend of $R_{2,IE}$ values in relation to myelin content persisted. However, the observed effect ($R_{2,IE}$) was relatively small and did not completely explain the experimental R_2 value changes caused

by variations in MVF (Figure 4.8C). This result implies that the effect of magnetic susceptibility of myelin maybe relatively small at 7T, and our experimental results are mostly explainable by the effect of $T_{2,0}$, the bulk water relaxation in Eq. (1) at 7T. In other words, results from Monte-Carlo simulations also supported mixing of IE water with myelin water signals, as susceptibility-induced T_2 decay in IE spaces was relatively small to fully explain the observed MVF related R_2 changes. Therefore, the combined experimental and simulation results, it can be suggested that myelin water containing short- T_2 components has a significant impact on ex vivo MRI- R_2 values, despite not being easily distinguishable from long- T_2 components.

4.4.4 Limitations

There are several limitations in our study. First, unlike in vivo studies, chemical fixation for ex vivo studies cause microstructural degeneration such as myelin sheath loosening and cell shrinkage [97]. Additionally, fixation and dehydration steps in sample preparation for TEM processing can cause morphological changes in biological sample [98]. Damage to myelin structure due to the points mentioned may affect MVF and MST and result in different myelin structure information from in vivo MRI data. Therefore, for a more accurate quantitative analysis of myelin in post-mortem studies, more advanced approaches considering the above factors are required for in vivo translations. Second, our TEM data did not cover the full ROI as in MRI. In this experiment, TEM analysis was performed under the assumption that the structure of myelin in the ROI of the same age group was relatively similar compared to the age-related variation, and when multi-exponential relaxation fitting process was performed using only the ROI analyzed by TEM, it was confirmed that the results were similar to those in Figure 4.4 (Figure 4.10). Third, our experiments were only analyzed with access to small portions (single slice acquisition) of WM regions within the brain, i.e., a limited MRI volume coverage. Therefore, it is thought that an approach to myelin changes in a wide range of WM areas through additional studies can provide deeper insights between MRI results and myelin changes. Finally, more accurate investigation of factors affecting T_2 measurement, such as the effect of iron concentration, is needed. Several studies have reported that T_2 is sensitive to iron, and iron deposition may occur in the WM, affecting T_2 analysis [10,11,99,100]. Of course, in our previous study, it was confirmed that the effect of myelin contents was dominant within the same ROI through magnetic susceptibility analysis [72], but for a more accurate analysis, it is desirable to additionally consider the effect of iron in future development.

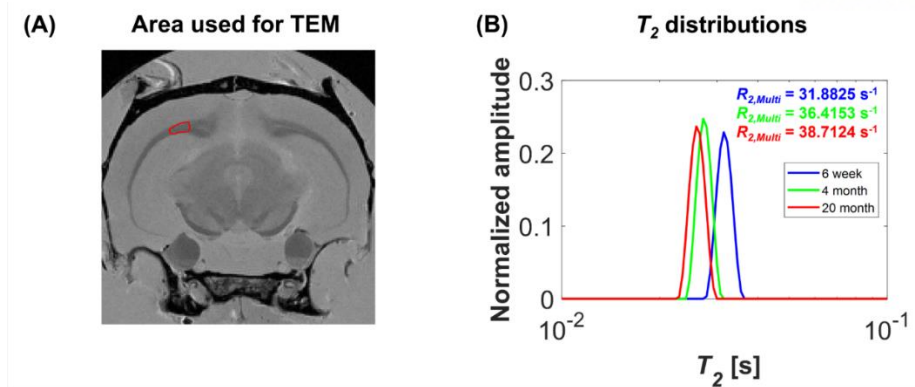


Figure 4.10. Multi-exponential relaxation fitting results using data in the TEM area. (A) ROI marking the TEM area (red) in proton density-weighted image. (B) T_2 distributions derived from the mean signal of the TEM area of each age group (Young: 6-week-1, Adult: 4-month-1, and Old: 20-month-2). $R_{2,Multi}$ values for each age group are color-coded (Young: blue, Adult: green, Old: red).

4.4.5 Conclusion

Utilizing multiple spin echo sequence-based MRI- R_2 measurements, this study assessed myelin changes in post-mortem aging rat CCs, alongside TEM- and simulation-based validation. The hypothesis was that absolute R_2 values may contain volumetric information of myelin, even with mono-exponential relaxation. The comparison between independent parameters from MRI, TEM, and simulations supports this suggestion. It was found that multiple spin echo sequence-based MRI- R_2 values in aging post-mortem rat CCs reflects the volumetric information of myelin, despite mono-exponential T_2 relaxation of myelin water signals. These results indicate that MRI- R_2 measurements at 7T can still provide quantitative information to assess myelin content in ex vivo conditions via conventional fixation methods without prolonged washings.

The original source of Chapter 4 is the article, Cho, H., Han, S., & Cho, H. J. (2023). Empirical relationship between TEM-derived myelin volume fraction and MRI- R_2 values in aging ex vivo rat corpus callosum. *Magnetic Resonance Imaging*, In revision.

Chapter 5. Conclusions

5.1 Summary

In this thesis, we aimed to quantify age-related changes in myelin volume in the CC region of the post-mortem rat brains through MRI-based measurements (R_1 , R_2 , and QSM) and histological and theoretical validation processes. It was confirmed that the absolute MVF values analyzed through TEM processing showed significant correlations with the values derived from each MRI measurements, and these tendency were further verified through simulation processing. These results suggest that the myelin volume information obtained through the mentioned MRI methods can be considered as an ex vivo MRI surrogate for MVF in post-mortem rat brain WM.

5.2 Limitations and Future works

This study is limited to measuring changes in myelin only within a small portions of the post-mortem rodent brain. As regional differences in myelin distribution exist within the WM, approaches to myelin changes in a wide range of WM areas should be considered to provide further insight into the relationship between MRI results and myelin changes. Additionally, for ex vivo study, biological samples may undergo microstructural degeneration due to chemical fixation, which may reflect different myelin structural information than in vivo MRI data. Therefore, further in vivo experimental designs with various MRI contrasts may provide new insights into the correlation between MRI and myelin. Lastly, for a more accurate analysis of the experimental values, factors such as iron deposition and water exchange between compartments that can sufficiently affect the experiment should be strictly considered. Paramagnetic iron can accumulate as the brain ages and can alter relaxation rates and magnetic susceptibility values. Water exchange between myelin and other compartments is also considered as a factor that may affect relaxation rate measurements. Therefore, it is desirable to additionally consider the influence of these factors in future development.

For future improvements in myelin quantification using MRI, we will approach myelin changes in various neurodegenerative disease models through in vivo and ex vivo experiments. For example, 5xFAD transgenic mice are characterized by rapidly progressing key features of Alzheimer's disease amyloid pathology and are expected to be very useful for evaluating amyloid-associated myelin degeneration using MRI. The establishment of various MRI techniques and histological/theoretical validation methods in neurodegenerative disease models is expected to be usefully applied to future clinical studies.

References

1. Sprawls, P. (2000). *Magnetic resonance imaging: principles, methods, and techniques*. Madison: Medical Physics Publishing.
2. Liu, C., Wei, H., Gong, N. J., Cronin, M., Dibb, R., & Decker, K. (2015). Quantitative susceptibility mapping: contrast mechanisms and clinical applications. *Tomography*, 1(1), 3-17.
3. Schweser, F., Deistung, A., & Reichenbach, J. R. (2016). Foundations of MRI phase imaging and processing for Quantitative Susceptibility Mapping (QSM). *Zeitschrift für medizinische Physik*, 26(1), 6-34.
4. Deber, C. M., & Reynolds, S. J. (1991). Central nervous system myelin: structure, function, and pathology. *Clinical biochemistry*, 24(2), 113-134.
5. Trapp, B. D., & Kidd, G. J. (2004). Structure of the myelinated axon. In *Myelin biology and disorders* (pp. 3-27). Academic Press.
6. van der Knaap, M. S., & Valk, J. (2005). Myelin and white matter. *Magnetic resonance of myelination and myelin disorders*, 1-19.
7. Min, Y., Kristiansen, K., Boggs, J. M., Husted, C., Zasadzinski, J. A., & Israelachvili, J. (2009). Interaction forces and adhesion of supported myelin lipid bilayers modulated by myelin basic protein. *Proceedings of the National Academy of Sciences*, 106(9), 3154-3159.
8. Salzer, J. L. (2015). Schwann cell myelination. *Cold Spring Harbor perspectives in biology*, 7(8), a020529.
9. Peters, A. (2002). The effects of normal aging on myelin and nerve fibers: a review. *Journal of neurocytology*, 31(8-9), 581-593.
10. Laule, C., Vavasour, I. M., Kolind, S. H., Li, D. K., Traboulsee, T. L., Moore, G. W., & MacKay, A. L. (2007). Magnetic resonance imaging of myelin. *Neurotherapeutics*, 4(3), 460-484.
11. MacKay, A. L., & Laule, C. (2016). Magnetic resonance of myelin water: an in vivo marker for myelin. *Brain plasticity*, 2(1), 71-91.
12. Heath, F., Hurley, S. A., Johansen-Berg, H., & Sampaio-Baptista, C. (2018). Advances in noninvasive myelin imaging. *Developmental neurobiology*, 78(2), 136-151.
13. van der Weijden, C. W., García, D. V., Borra, R. J., Thurner, P., Meilof, J. F., van Laar, P. J., ... & de Vries, E. F. (2021). Myelin quantification with MRI: A systematic review of accuracy and

reproducibility. *Neuroimage*, 226, 117561.

14. Schmierer, K., Wheeler-Kingshott, C.A., Tozer, D. J., Boulby, P.A., Parkes, H. G., Yousry, T. A., ... & Miller, D. H. (2008). Quantitative magnetic resonance of postmortem multiple sclerosis brain before and after fixation. *Magnetic Resonance in Medicine: An Official Journal of the International Society for Magnetic Resonance in Medicine*, 59(2), 268-277.

15. Laule, C., Leung, E., Li, D. K., Traboulsee, A. L., Paty, D. W., MacKay, A. L., & Moore, G. R. (2006). Myelin water imaging in multiple sclerosis: quantitative correlations with histopathology. *Multiple Sclerosis Journal*, 12(6), 747-753.

16. Soustelle, L., Antal, M. C., Lamy, J., Rousseau, F., Armspach, J. P., & Loureiro de Sousa, P. (2019). Correlations of quantitative MRI metrics with myelin basic protein (MBP) staining in a murine model of demyelination. *NMR in Biomedicine*, 32(9), e4116.

17. Stüber, C., Morawski, M., Schäfer, A., Labadie, C., Wähnert, M., Leuze, C., ... & Turner, R. (2014). Myelin and iron concentration in the human brain: a quantitative study of MRI contrast. *Neuroimage*, 93, 95-106.

18. Lutti, A., Dick, F., Sereno, M. I., & Weiskopf, N. (2014). Using high-resolution quantitative mapping of R1 as an index of cortical myelination. *Neuroimage*, 93, 176-188.

19. Li, W., Wu, B., Batrachenko, A., Bancroft-Wu, V., Morey, R. A., Shashi, V., ... & Liu, C. (2014). Differential developmental trajectories of magnetic susceptibility in human brain gray and white matter over the lifespan. *Human brain mapping*, 35(6), 2698-2713.

20. Argyridis, I., Li, W., Johnson, G. A., & Liu, C. (2014). Quantitative magnetic susceptibility of the developing mouse brain reveals microstructural changes in the white matter. *Neuroimage*, 88, 134-142.

21. Lodygensky, G. A., Marques, J. P., Maddage, R., Perroud, E., Sizonenko, S. V., Hüppi, P. S., & Gruetter, R. (2012). In vivo assessment of myelination by phase imaging at high magnetic field. *Neuroimage*, 59(3), 1979-1987.

22. Stahon, K. E., Bastian, C., Griffith, S., Kidd, G. J., Brunet, S., & Baltan, S. (2016). Age-related changes in axonal and mitochondrial ultrastructure and function in white matter. *Journal of Neuroscience*, 36(39), 9990-10001.

23. Xie, F., Liang, P., Fu, H., Zhang, J. C., & Chen, J. (2014). Effects of normal aging on myelin sheath ultrastructures in the somatic sensorimotor system of rats. *Molecular Medicine Reports*, 10(1), 459-466.

24. Lee, D., Han, S., & Cho, H. (2017). Optimization of sparse phase encodings for variable repetition-

delay turbo-spin echo (TSE) T1 measurements for preclinical applications. *Journal of Magnetic Resonance*, 274, 57-64.

25. De Rochefort, L., Brown, R., Prince, M. R., & Wang, Y. I. (2008). Quantitative MR susceptibility mapping using piece-wise constant regularized inversion of the magnetic field. *Magnetic Resonance in Medicine: An Official Journal of the International Society for Magnetic Resonance in Medicine*, 60(4), 1003-1009.

26. Schofield, M. A., & Zhu, Y. (2003). Fast phase unwrapping algorithm for interferometric applications. *Optics letters*, 28(14), 1194-1196.

27. Zhou, D., Liu, T., Spincemaille, P., & Wang, Y. (2014). Background field removal by solving the Laplacian boundary value problem. *NMR in Biomedicine*, 27(3), 312-319.

28. Liu, J., Liu, T., de Rochefort, L., Ledoux, J., Khalidov, I., Chen, W., ... & Wang, Y. (2012). Morphology enabled dipole inversion for quantitative susceptibility mapping using structural consistency between the magnitude image and the susceptibility map. *Neuroimage*, 59(3), 2560-2568.

29. Barazany, D., Basser, P. J., & Assaf, Y. (2009). In vivo measurement of axon diameter distribution in the corpus callosum of rat brain. *Brain*, 132(5), 1210-1220.

30. Zaimi, A., Wabartha, M., Herman, V., Antonsanti, P. L., Perone, C. S., & Cohen-Adad, J. (2018). AxonDeepSeg: automatic axon and myelin segmentation from microscopy data using convolutional neural networks. *Scientific reports*, 8(1), 3816.

31. Pathak, A. P., Ward, B. D., & Schmainda, K. M. (2008). A novel technique for modeling susceptibility-based contrast mechanisms for arbitrary microvascular geometries: the finite perturber method. *Neuroimage*, 40(3), 1130-1143.

32. Wang, Y., & Liu, T. (2015). Quantitative susceptibility mapping (QSM): decoding MRI data for a tissue magnetic biomarker. *Magnetic resonance in medicine*, 73(1), 82-101.

33. Sati, P., van Gelderen, P., Silva, A. C., Reich, D. S., Merkle, H., De Zwart, J. A., & Duyn, J. H. (2013). Micro-compartment specific T2* relaxation in the brain. *Neuroimage*, 77, 268-278.

34. Sun, H., Kate, M., Gioia, L. C., Emery, D. J., Butcher, K., & Wilman, A. H. (2016). Quantitative susceptibility mapping using a superposed dipole inversion method: application to intracranial hemorrhage. *Magnetic resonance in medicine*, 76(3), 781-791.

35. Wharton, S., & Bowtell, R. (2012). Fiber orientation-dependent white matter contrast in gradient echo MRI. *Proceedings of the National Academy of Sciences*, 109(45), 18559-18564.

36. Kim, J. H., & Juraska, J. M. (1997). Sex differences in the development of axon number in the splenium of the rat corpus callosum from postnatal day 15 through 60. *Developmental brain research*, 102(1), 77-85.
37. Yates, M. A., & Juraska, J. M. (2007). Increases in size and myelination of the rat corpus callosum during adulthood are maintained into old age. *Brain research*, 1142, 13-18.
38. Li, C., Zhang, L., Ma, Q., Tang, Y., & He, Y. (2017). Stereological evidence for de/re-generation of myelin sheaths in aged brain white matter of female rats. *Image Analysis & Stereology*, 36(2), 111-120.
39. Lee, J., Shmueli, K., Fukunaga, M., Van Gelderen, P., Merkle, H., Silva, A. C., & Duyn, J. H. (2010). Sensitivity of MRI resonance frequency to the orientation of brain tissue microstructure. *Proceedings of the National Academy of Sciences*, 107(11), 5130-5135.
40. Liu, C. (2010). Susceptibility tensor imaging. *Magnetic Resonance in Medicine: An Official Journal of the International Society for Magnetic Resonance in Medicine*, 63(6), 1471-1477.
41. Duyn, J. H. (2018). Studying brain microstructure with magnetic susceptibility contrast at high-field. *Neuroimage*, 168, 152-161.
42. Hallgren, B., & Sourander, P. (1958). The effect of age on the non-haemin iron in the human brain. *Journal of neurochemistry*, 3(1), 41-51.
43. Raz, E., Branson, B., Jensen, J. H., Bester, M., Babb, J. S., Herbert, J., ... & Inglese, M. (2015). Relationship between iron accumulation and white matter injury in multiple sclerosis: a case-control study. *Journal of neurology*, 262, 402-409.
44. Acosta-Cabronero, J., Betts, M. J., Cardenas-Blanco, A., Yang, S., & Nestor, P. J. (2016). In vivo MRI mapping of brain iron deposition across the adult lifespan. *Journal of Neuroscience*, 36(2), 364-374.
45. Thomas, L. O., Boyko, O. B., Anthony, D. C., & Burger, P. C. (1993). MR detection of brain iron. *American Journal of Neuroradiology*, 14(5), 1043-1048.
46. Haacke, E. M., Cheng, N. Y., House, M. J., Liu, Q., Neelavalli, J., Ogg, R. J., ... & Obenaus, A. (2005). Imaging iron stores in the brain using magnetic resonance imaging. *Magnetic resonance imaging*, 23(1), 1-25.
47. Kamman, R. L., Go, K. G., Stomp, G. P., Hulstaert, C. E., & Berendsen, H. J. C. (1985). Changes of relaxation times T1 and T2 in rat tissues after biopsy and fixation. *Magnetic resonance imaging*, 3(3), 245-250.

48. Birkel, C., Langkammer, C., Golob-Schwarzl, N., Leoni, M., Haybaeck, J., Goessler, W., ... & Ropele, S. (2016). Effects of formalin fixation and temperature on MR relaxation times in the human brain. *NMR in Biomedicine*, 29(4), 458-465.
49. Shatil, A. S., Uddin, M. N., Matsuda, K. M., & Figley, C. R. (2018). Quantitative ex vivo MRI changes due to progressive formalin fixation in whole human brain specimens: longitudinal characterization of diffusion, relaxometry, and myelin water fraction measurements at 3T. *Frontiers in medicine*, 5, 31.
50. Luo, J., He, X., & Yablonskiy, D. A. (2014). Magnetic susceptibility induced white matter MR signal frequency shifts—experimental comparison between Lorentzian sphere and generalized Lorentzian approaches. *Magnetic resonance in medicine*, 71(3), 1251-1263.
51. O'callaghan, J., Holmes, H., Powell, N., Wells, J. A., Ismail, O., Harrison, I. F., ... & Lythgoe, M. F. (2017). Tissue magnetic susceptibility mapping as a marker of tau pathology in Alzheimer's disease. *Neuroimage*, 159, 334-345.
52. Kan, H., Uchida, Y., Arai, N., Takizawa, M., Miyati, T., Kunitomo, H., ... & Shibamoto, Y. (2020). Decreasing iron susceptibility with temperature in quantitative susceptibility mapping: A phantom study. *Magnetic Resonance Imaging*, 73, 55-61.
53. Langkammer, C., Schweser, F., Krebs, N., Deistung, A., Goessler, W., Scheurer, E., ... & Reichenbach, J. R. (2012). Quantitative susceptibility mapping (QSM) as a means to measure brain iron? A post mortem validation study. *Neuroimage*, 62(3), 1593-1599.
54. Fields, R. D. (2008). White matter matters. *Scientific American*, 298(3), 54-61.
55. Kerman, B. E., Kim, H. J., Padmanabhan, K., Mei, A., Georges, S., Joens, M. S., ... & Gage, F. H. (2015). In vitro myelin formation using embryonic stem cells. *Development*, 142(12), 2213-2225.
56. Horch, R. A., Gore, J. C., & Does, M. D. (2011). Origins of the ultrashort-T2 1H NMR signals in myelinated nerve: a direct measure of myelin content?. *Magnetic resonance in medicine*, 66(1), 24-31.
57. Sheth, V., Shao, H., Chen, J., Vandenberg, S., Corey-Bloom, J., Bydder, G. M., & Du, J. (2016). Magnetic resonance imaging of myelin using ultrashort Echo time (UTE) pulse sequences: Phantom, specimen, volunteer and multiple sclerosis patient studies. *Neuroimage*, 136, 37-44.
58. Piredda, G. F., Hilbert, T., Thiran, J. P., & Kober, T. (2021). Probing myelin content of the human brain with MRI: A review. *Magnetic resonance in medicine*, 85(2), 627-652.
59. Mackay, A., Whittall, K., Adler, J., Li, D., Paty, D., & Graeb, D. (1994). In vivo visualization of

- myelin water in brain by magnetic resonance. *Magnetic resonance in medicine*, 31(6), 673-677.
60. Carr, H. Y., & Purcell, E. M. (1954). Effects of diffusion on free precession in nuclear magnetic resonance experiments. *Physical review*, 94(3), 630.
61. Meiboom, S., & Gill, D. (1958). Modified spin-echo method for measuring nuclear relaxation times. *Review of scientific instruments*, 29(8), 688-691.
62. Whittall, K. P., & MacKay, A. L. (1989). Quantitative interpretation of NMR relaxation data. *Journal of Magnetic Resonance (1969)*, 84(1), 134-152.
63. Webb, S., Munro, C. A., Midha, R., & Stanisz, G. J. (2003). Is multicomponent T2 a good measure of myelin content in peripheral nerve?. *Magnetic Resonance in Medicine: An Official Journal of the International Society for Magnetic Resonance in Medicine*, 49(4), 638-645.
64. Kozlowski, P., Liu, J., Yung, A. C., & Tetzlaff, W. (2008). High-resolution myelin water measurements in rat spinal cord. *Magnetic Resonance in Medicine: An Official Journal of the International Society for Magnetic Resonance in Medicine*, 59(4), 796-802.
65. Harkins, K. D., Dula, A. N., & Does, M. D. (2012). Effect of intercompartmental water exchange on the apparent myelin water fraction in multiexponential T2 measurements of rat spinal cord. *Magnetic resonance in medicine*, 67(3), 793-800.
66. Does, M. D., & Gore, J. C. (2002). Compartmental study of T1 and T2 in rat brain and trigeminal nerve in vivo. *Magnetic Resonance in Medicine: An Official Journal of the International Society for Magnetic Resonance in Medicine*, 47(2), 274-283.
67. Thiessen, J. D., Zhang, Y., Zhang, H., Wang, L., Buist, R., Del Bigio, M. R., ... & Martin, M. (2013). Quantitative MRI and ultrastructural examination of the cuprizone mouse model of demyelination. *NMR in Biomedicine*, 26(11), 1562-1581.
68. West, K. L., Kelm, N. D., Carson, R. P., Gochberg, D. F., Ess, K. C., & Does, M. D. (2018). Myelin volume fraction imaging with MRI. *Neuroimage*, 182, 511-521.
69. Schmierer, K., Scaravilli, F., Barker, G. J., Gordon, R., MacManus, D. G., & Miller, D. H. (2003). Stereotactic co-registration of magnetic resonance imaging and histopathology in post-mortem multiple sclerosis brain. *Neuropathology and applied neurobiology*, 29(6), 596-601.
70. Shepherd, T. M., Thelwall, P. E., Stanisz, G. J., & Blackband, S. J. (2009). Aldehyde fixative solutions alter the water relaxation and diffusion properties of nervous tissue. *Magnetic Resonance in Medicine: An Official Journal of the International Society for Magnetic Resonance in Medicine*, 62(1),

26-34.

71. Dawe, R. J., Bennett, D. A., Schneider, J. A., Vasireddi, S. K., & Arfanakis, K. (2009). Postmortem MRI of human brain hemispheres: T2 relaxation times during formaldehyde fixation. *Magnetic Resonance in Medicine: An Official Journal of the International Society for Magnetic Resonance in Medicine*, 61(4), 810-818.
72. Cho, H., Lee, H., Gong, Y., Kim, Y. R., Cho, J., & Cho, H. J. (2022). Quantitative susceptibility mapping and R1 measurement: Determination of the myelin volume fraction in the aging ex vivo rat corpus callosum. *NMR in Biomedicine*, 35(3), e4645.
73. Paxinos, G., & Watson, C. (2006). *The rat brain in stereotaxic coordinates: hard cover edition*. Elsevier.
74. Paxinos, G., Watson, C., Calabrese, E., Badea, A., & Johnson, G. A. (2015). *MRI/DTI atlas of the rat brain*. Academic Press.
75. Kosior, R. K., Lauzon, M. L., Federico, P., & Frayne, R. (2011). Algebraic T2 estimation improves detection of right temporal lobe epilepsy by MR T2 relaxometry. *Neuroimage*, 58(1), 189-197.
76. Milford, D., Rosbach, N., Bendszus, M., & Heiland, S. (2015). Mono-exponential fitting in T2-relaxometry: relevance of offset and first echo. *PloS one*, 10(12), e0145255.
77. Alonso-Ortiz, E., Levesque, I. R., & Pike, G. B. (2015). MRI-based myelin water imaging: a technical review. *Magnetic resonance in medicine*, 73(1), 70-81.
78. Does, M. Multi-Exponential Relaxation Analysis (MERA) Toolbox, Version 2. 2014.
79. Hildebrand, T., & Rüeeggsegger, P. (1997). A new method for the model-independent assessment of thickness in three-dimensional images. *Journal of microscopy*, 185(1), 67-75.
80. Dougherty, R., & Kunzelmann, K. H. (2007). Computing local thickness of 3D structures with ImageJ. *Microscopy and Microanalysis*, 13(S02), 1678-1679.
81. Doube, M., Kłosowski, M. M., Arganda-Carreras, I., Cordelières, F. P., Dougherty, R. P., Jackson, J. S., ... & Shefelbine, S. J. (2010). BoneJ: free and extensible bone image analysis in ImageJ. *Bone*, 47(6), 1076-1079.
82. Abràmoff, M. D., Magalhães, P. J., & Ram, S. J. (2004). Image processing with ImageJ. *Biophotonics international*, 11(7), 36-42.
83. Kleinberg, R. L., & Horsfield, M. A. (1990). Transverse relaxation processes in porous sedimentary

rock. *Journal of Magnetic Resonance* (1969), 88(1), 9-19.

84. Ronczka, M., & Müller-Petke, M. (2012). Optimization of CPMG sequences to measure NMR transverse relaxation time T₂ in borehole applications. *Geoscientific Instrumentation, Methods and Data Systems*, 1(2), 197-208.

85. Rosenblatt, C. H. A. R. L. E. S., Yager, P. A. U. L., & Schoen, P. E. (1987). Orientation of lipid tubules by a magnetic field. *Biophysical journal*, 52(2), 295-301.

86. Li, W., Wu, B., Avram, A. V., & Liu, C. (2012). Magnetic susceptibility anisotropy of human brain in vivo and its molecular underpinnings. *Neuroimage*, 59(3), 2088-2097.

87. Xu, T., Foxley, S., Kleinnijenhuis, M., Chen, W. C., & Miller, K. L. (2018). The effect of realistic geometries on the susceptibility-weighted MR signal in white matter. *Magnetic resonance in medicine*, 79(1), 489-500.

88. Hédouin, R., Metere, R., Chan, K. S., Licht, C., Mollink, J., Van Walsum, A. M. C., & Marques, J. P. (2021). Decoding the microstructural properties of white matter using realistic models. *NeuroImage*, 237, 118138.

89. Li, W., Liu, C., Duong, T. Q., van Zijl, P. C., & Li, X. (2017). Susceptibility tensor imaging (STI) of the brain. *NMR in Biomedicine*, 30(4), e3540.

90. Holz, M., Heil, S. R., & Sacco, A. (2000). Temperature-dependent self-diffusion coefficients of water and six selected molecular liquids for calibration in accurate ¹H NMR PFG measurements. *Physical Chemistry Chemical Physics*, 2(20), 4740-4742.

91. Dusek, P., Madai, V. I., Huelnhagen, T., Bahn, E., Matej, R., Sobesky, J., ... & Wuerfel, J. (2019). The choice of embedding media affects image quality, tissue R₂^{*}, and susceptibility behaviors in post-mortem brain MR microscopy at 7.0 T. *Magnetic Resonance in Medicine*, 81(4), 2688-2701.

92. Fox, C. H., Johnson, F. B., Whiting, J., & Roller, P. P. (1985). Formaldehyde fixation. *Journal of Histochemistry & Cytochemistry*, 33(8), 845-853.

93. Alrafiah, A., & Alshali, R. (2019). The effect of prolonged formalin fixation on the staining characteristics of archival human brain tissue. *Folia Morphologica*, 78(2), 230-236.

94. Moore, G. R. W., Leung, E., MacKay, A. L., Vavasour, I. M., Whittall, K. P., Cover, K. S., ... & Paty, D. W. (2000). A pathology-MRI study of the short-T₂ component in formalin-fixed multiple sclerosis brain. *Neurology*, 55(10), 1506-1510.

95. Seifert, A. C., Umphlett, M., Hefti, M., Fowkes, M., & Xu, J. (2019). Formalin tissue fixation biases myelin-sensitive MRI. *Magnetic resonance in medicine*, 82(4), 1504-1517.
96. Dula, A. N., Gochberg, D. F., Valentine, H. L., Valentine, W. M., & Does, M. D. (2010). Multiexponential T2, magnetization transfer, and quantitative histology in white matter tracts of rat spinal cord. *Magnetic Resonance in Medicine: An Official Journal of the International Society for Magnetic Resonance in Medicine*, 63(4), 902-909.
97. Chen, H. S. M., Holmes, N., Liu, J., Tetzlaff, W., & Kozlowski, P. (2017). Validating myelin water imaging with transmission electron microscopy in a rat spinal cord injury model. *NeuroImage*, 153, 122-130.
98. Zhang, Y., Huang, T., Jorgens, D. M., Nickerson, A., Lin, L. J., Pelz, J., ... & Nan, X. (2017). Quantitating morphological changes in biological samples during scanning electron microscopy sample preparation with correlative super-resolution microscopy. *PloS one*, 12(5), e0176839.
99. Langkammer, C., Krebs, N., Goessler, W., Scheurer, E., Ebner, F., Yen, K., ... & Ropele, S. (2010). Quantitative MR imaging of brain iron: a postmortem validation study. *Radiology*, 257(2), 455-462.
100. Schipper, H. M. (2012). Neurodegeneration with brain iron accumulation—clinical syndromes and neuroimaging. *Biochimica et Biophysica Acta (BBA)-Molecular Basis of Disease*, 1822(3), 350-360.

Acknowledgements

I would like to take this opportunity to express my gratitude to those who helped me to successfully complete my MS-PhD course.

First of all, I would like to express my deepest gratitude to my supervisor, Hyung Joon Cho, who guided me to the path of a researcher and gave me generous encouragement and help during my MS-PhD course. His passion and attitude towards research impressed me and motivated me to become an independent researcher.

I would like to express my sincere thanks to my thesis committee members, Professor Taejoon Kwon, Professor Jung-Hoon Park, Professor Joon-Mo Yang, and Professor Kwangyeol Baek for their thoughtful advice and feedbacks on this thesis.

I would like to express my sincere gratitude to Dr. Seokha Jin for his many academic guidance and thoughtful help in various fields. It was a great fortune for me to be able to do research together during my MS-PhD course.

I would like to express my appreciation to our BISE laboratory members for their thoughtful help and advice. While researching with them, I was able to prepare a stepping stone for academic growth, and their kindness and consideration were a great source of strength for me.

I sincerely thank my family for their unwavering support and encouragement over a long period of time. I am grateful to my parents who gave birth to me, raised me, and give me great love even now. And I sincerely thank my older sister for always giving me sincere advice. Without their help, I would not have completed my MS-PhD course.

Finally, I would like to say thank you to my friends. They have always been the best for me and I hope we all succeed together.